# $^{139}$La NMR Charge Order Study of $La_{2-x}Sr_xCuO_4$

# $^{139}$La NMR Charge Order Study of $La_{2-x}Sr_xCuO_4$

By Alexandre Arsenault,

*A Thesis Submitted to the School of Graduate Studies in the Partial Fulfillment of the Requirements for the Degree Masters of Science*

McMaster University

Masters of Science (2018)

Hamilton, Ontario (Department of Physics)

TITLE: $^{139}$La NMR Charge Order Study of $La_{2-x}Sr_xCuO_4$

AUTHOR: Alexandre Arsenault (McMaster University)

SUPERVISOR: Dr. Takashi Imai

NUMBER OF PAGES: 1, 77

# Abstract

Although charge order was discovered in $La_{1.6-x}Nd_{0.4}Sr_xCuO_4$ over two decades ago, this elusive state has not been as easily observable in $La_{2-x}Sr_xCuO_4$. $^{63}$Cu NMR experiments demonstrated that $La_{2-x}Sr_xCuO_4$ did indeed transition into a charge ordering state, but the lack of evidence in other experiments made many physicists doubtful of its presence. With recent advancements in technology, x-ray scattering experiments have finally been able to measure charge order Bragg peaks in $La_{2-x}Sr_xCuO_4$, proving that charge order anomalies seen by $^{63}$Cu NMR was legitimate. More recent $^{63}$Cu NMR showed that a broad wing-like signal emerges when charge order sets in in $La_{1.885}Sr_{0.115}CuO_4$ with a much faster relaxation rate than the normal signal. In this thesis, we attempt to revisit the charge ordered state of $La_{2-x}Sr_xCuO_4$ by measuring $^{139}$La NMR on single crystals of x = 0.13, 0.115 and 0.10. By splitting the relaxation rate into two components, we were able to determine the temperature at which a fast component emerges, corresponding to the same temperature recorded by $^{63}$Cu NMR and x-ray scattering for the same $La_{1.885}Sr_{0.115}CuO_4$ crystal. Using this method, we measured $^{139}$La NMR lineshapes and spin-lattice relaxation rates and mapped out the charge order dome of the phase diagram of $La_{2-x}Sr_xCuO_4$.

# *Acknowledgements*

I would first like to acknowledge my advisor, Dr. Takashi Imai, for his academic and knowledgable support throught this thesis. Dr. Imai's high standards have influenced me to work harder to achieve the best results possible. Thanks to Dr. Paul Dube for taking care of the helium liquefier and SQUID and thanks to Dr. Fujita at Tohoku University for the sample preparation and Dr. Lee's group at Stanford University for the collaboration. I would also like to thank my coworkers and good friends Sean Takahashi and Jerry Wang for help in the lab and pleasant conversations.

I cannot enumerate all the amiable people I have met in Hamilton, but I would like to specifically thank my roomates and good friends James Lambert, Wyatt Kirkby and Joey Rucska for the enjoyable two years. I would also like to thank Lili Zhang for the good times.

Finally, I'm very greatful for my friends and family back in Montreal for always being there and supporting me. I would not have been able to do this thesis without their unconditional support.

# Contents

# List of Figures

# List of Tables

# Chapter 1

# Introduction

## 1.1 The High-$T_c$ Cuprates

In 1949, Mott proposed that certain materials, now called Mott insulators, would not conduct even with a half filled conduction band due to Coulomb repulsion [1]. Nearly four decades later, in 1986, a doped Mott insulator was found to be superconducting in $La_{2-x}Ba_xCuO_4$ [2]. This marked the craze of the high critical temperature, high-$T_c$, cuprates, where many physicists gravitated towards solving the mysterious mechanism of unconventional superconductivity and many different cuprate samples were discovered [3].

Superconductivity describes a material which has both perfect conductivity and diamagnetism. This can be utilized in many ways, such as magnetic levitation and in magnetic resonance imaging, where magnetic fields of up to 3 T are typically used [4]. Although Bardeen-Cooper-Schrieffer, BCS, theory can perfectly model conventional superconductors such as pure metals, it is still unclear if BCS can

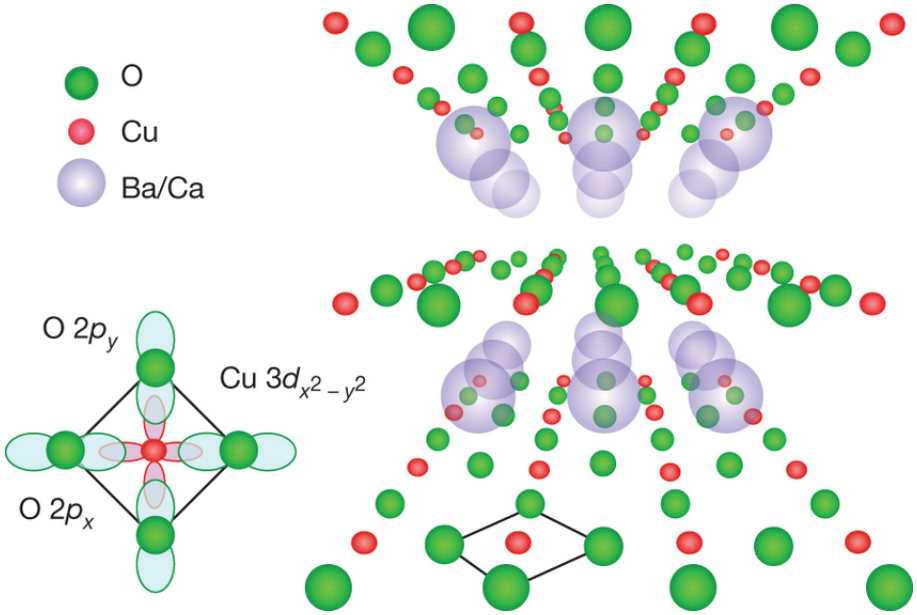


FIGURE 1.1: Perovskite structure of typical cuprate superconductors. The $CuO_2$ planes in green and red host the Cooper pairs responsible for superconductivity. The overlap of orbitals on the left shows how conductivity is enabled in the $CuO_2$ planes. Image taken from [6] with the copyright permission shown in the Appendix.

explain high-$T_c$ materials, since the pairing mechanism may differ from phonon-mediated electron-electron interactions. Thus, more work is needed in developing the theory for the mysterious high-$T_c$'s.

With extensive experimental work on the cuprates, it was found that the key to superconductivity in the cuprates lies in the $CuO_2$ planes [5], where holes form Cooper pairs inducing superconductivity. A typical cuprate structure is shown in Fig. 1.1, consisting of a layered perovskite structure with $CuO_2$ planes separated by blocking layers.

When the structure is undoped with carriers, the copper oxide planes have one hole per unit cell and are Mott insulators. The undoped compound is called

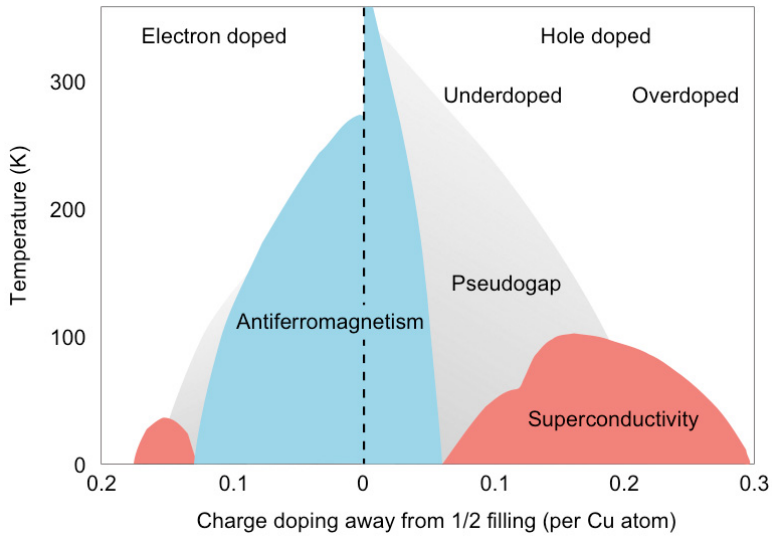


FIGURE 1.2: Typical phase diagram of hole and electron doped cuprates. All cuprates exhibit antiferromagnetic behaviour at low doping, while having a superconducting dome near x $\sim$ 0.15. Image obtained from [7].

the parent compound, such as $La_2CuO_4$ for $La_{2-x}Sr_xCuO_4$. Doping the parent compound with holes or electrons changes the number of holes per unit cell, causing the material to conduct at certain doping concentrations and temperatures. The cuprates undergo a number of different phase transitions depending on doping and temperature, as seen by the typical phase diagram shown in Fig. 1.2. The undoped parent compounds are antiferromagnetic, while doping with either holes or electrons creates a superconducting dome and pseudogap region. The pseudogap region is not well understood, but it consists of a phase where partial gaps form in the Fermi surface without inducing superconductivity.

The doping concentration resulting in the highest superconducting critical temperature is referred to as the optimal doping at x $\sim$ 0.15, while higher and lower dopings are called overdoped and underdoped, respectively. An interesting feature

of the hole doped superconducting dome is the dip at x $\sim$ 1/8, which coincides with the appearence of stripe order, a particular alignment of both charge and spin in the lattice. An early proposal of stripe ordering is shown in Fig. 1.3, where spins and holes form wave-like patterns on Cu sites, referred independently as spin and charge order, respectively, with spin ordering being initially found in $La_{2-x}Ba_xCuO_4$ [8]. First discovered in $La_{1.6-x}Nd_{0.4}Sr_xCuO_4$ two decades ago [9–11], recent progress has shown that charge order is also present in other cuprates such as $La_{1.8-x}Eu_{0.2}Sr_xCuO_4$ and $YBa_2Cu_3O_y$. This occurs below a certain temperature near x $\sim$ 1/8 doping. The stripe order brings many questions about the role of magnetism in high-$T_c$ superconductivity and has led to much speculation about the superconducting mechanism of the cuprates.

## 1.2 $La_{2-x}Sr_xCuO_4$ Structure

$La_{2-x}Sr_xCuO_4$ and related cuprates have a distinct $K_2NiF_4$-type crystal structure and undergo structural phase transitions at different temperatures depending on doping concentration. $La_{2-x}Sr_xCuO_4$ with x $\sim$ 1/8 is in a high temperature tetragonal (HTT) phase at room temperature, shown in Fig. 1.4(a). Lowering the temperature tilts the $CuO_6$ octahedra along the diagonal of the squares formed by the Cu atoms. This creates an orthorhombic structure, referred to as the low temperature orthorhombic (LTO) shown in Fig. 1.4(b). When $La^{(3+)}$ ions are substituted by $Nd^{(3+)}$ or $Eu^{(3+)}$ ions, an additional structural phase transition from the LTO to a low temperature tetragonal (LTT) phase takes place. However, merely one structural phase transition has been observed for $La_{2-x}Sr_xCuO_4$. Some

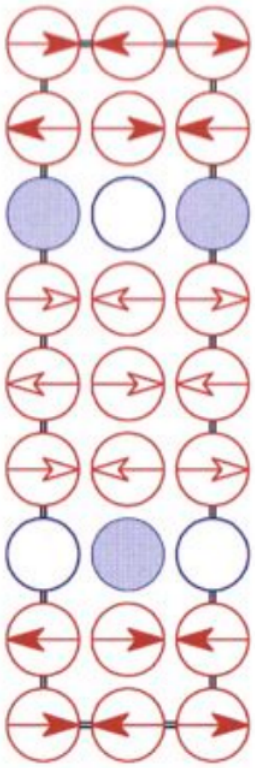

FIGURE 1.3: Diagram showing the stripe ordered phase of the cuprates. The oxygen atoms have been removed for clarity and only the Cu atoms are shown. The arrows denote the orientation of copper spins, with filled arrows showing the 180 degree rotation of spins along the hole river at the antiphase boundaries consisting of zero ordered moments. The filled blue circles represent holes localized on the copper atom. The double lines mark the magnetic unit cell. Image reproduced from [12]. Copyright permission shown in the Appendix.

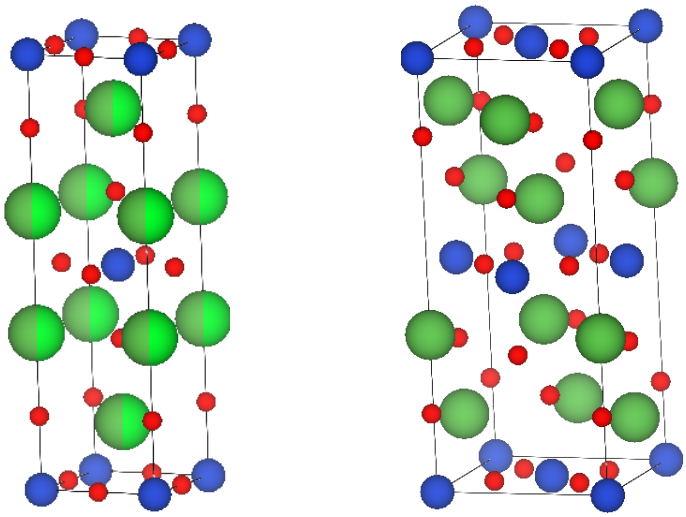

(a) (b)

FIGURE 1.4: (a) High temperature tetragonal structure of the parent compound $La_2CuO_4$. Green, red and blue spheres represent La, O and Cu atoms, respectively. Sr atoms are substituted for La ones in $La_{2-x}Sr_xCuO_4$. (b) Low temperature orthorhombic structure of $La_2CuO_4$.

experiments show that slight LTT tilting may be present even without $Nd^{(3+)}$ or $Eu^{(3+)}$ substitution [13], but more work is needed to confirm this observation. Due to charge order being pinned by the LTT structural phase transition in other cuprates, there is speculation that $La_{2-x}Sr_xCuO_4$ might also possess a dynamic LTT phase.

## 1.3 Properties of $La_{2-x}Sr_xCuO_4$

The superconducting critical temperature of the three different dopings of $La_{2-x}Sr_xCuO_4$ single crystals was measured using a Superconducting Quantum Interference Device, SQUID, at zero external magnetic field. The SQUID is one

of the most precise instrument used in physics and measures the magnetization of the sample by converting the magnetic flux of the sample to a voltage. As the crystal undergoes the superconducting transition, the magnetic flux created by the superconducting magnet is repelled and the magnetization of the sample becomes negative, as shown in Fig. 1.5. $T_c$ obtained from the SQUID was 34.5 K, 28 K, and 27.5 K for x = 0.13, 0.115, and 0.10, respectively.

Furthermore, transport measurements of $La_{2-x}Sr_xCuO_4$ have observed charge localization below the optimal stripe order dopings of x $\sim$ 0.12 [14]. By doping $La_{2-x}Sr_xCuO_4$ with 2% Zn to suppress superconductivity, the resistivity was found to be metallic ($\delta\rho/\delta T > 0$) at high temperatures and insulating ($\delta\rho/\delta T < 0$) at low temperatures. Although the charge localization temperature, $T_{loc}$, reaches a local maximum at x $\sim$ 1/8, it increases with decreasing doping near x $\sim$ 0.10, as shown in Fig. 1.6. Thus, the signatures of charge order are blurred by the presence of charge localization in $La_{2-x}Sr_xCuO_4$ below x $\sim$ 1/8, as described in the following sections.

Finally, an important feature of $La_{2-x}Sr_xCuO_4$ and other cuprates is the anisotropy of the upper critical field, $H_{c2}$. Type-II superconductors have two different critical fields. The lower critical field, $H_{c1}$, is the magnetic field strength at which vortices form and the magnetic field penetrates through the sample. The upper critical field, $H_{c2}$, corresponds to the field where superconductivity is fully suppressed. The critical field is highest where $T_c$ is at a maximum, near x $\sim$ 15%, but this changes depending on the field orientation. Due to the quasi two-dimensional nature of the superconductivity in the $CuO_2$ planes of $La_{2-x}Sr_xCuO_4$, a stronger field is needed to kill superconductivity when applied parallel to these planes rather

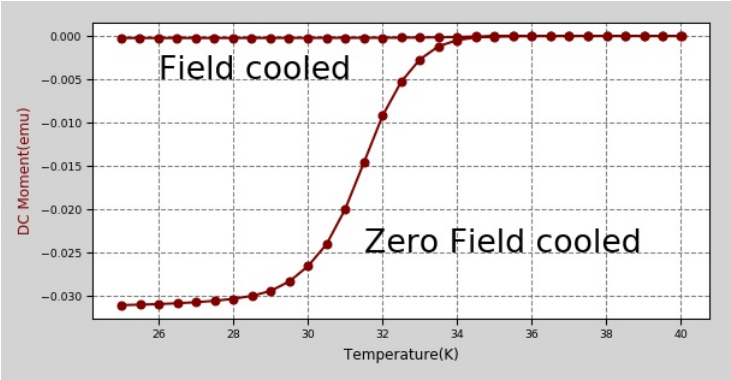


(a)

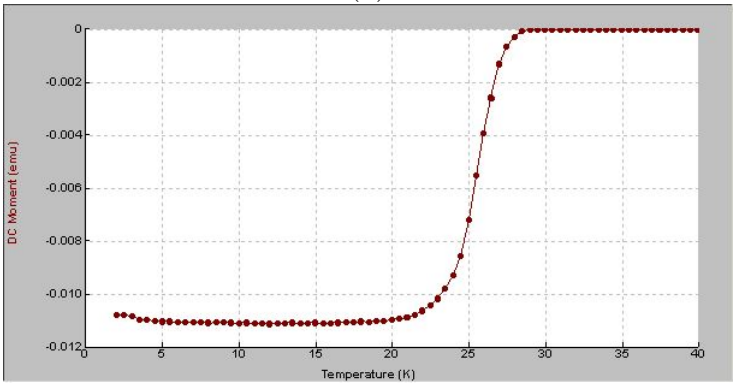


(b)

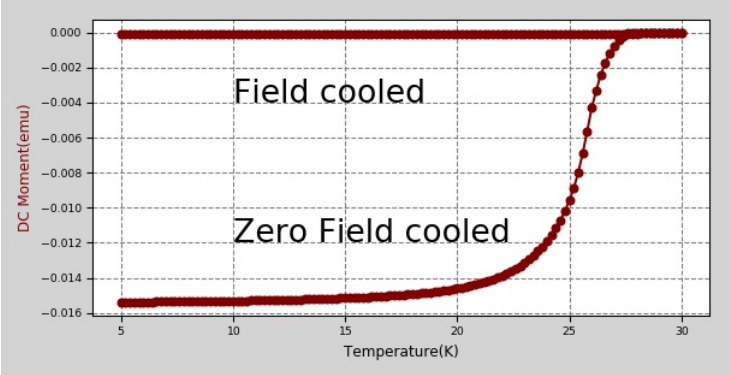


(c)

FIGURE 1.5: SQUID measurements for (a) x = 0.13, (b) x = 0.115 and (c) x = 0.10. The long moment deviates from 0 at the critical temperature of $T_c \sim 34.5$ K, $\sim 28$ K and $\sim 27.5$ K for x = 0.13, 0.115 and 0.10, respectively. For 10% and 13%, both zero field and field cooled measurements were taken and both agree on the critical temperature. Measurements obtained by Dr. Paul Dubé for 10% and 13% and Dr. Young Lee's group for 11.5%.

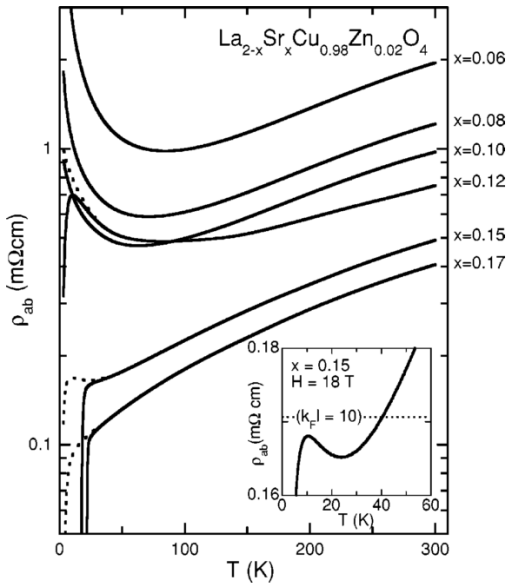


FIGURE 1.6: In-plane resistivity, $\rho_{ab}$, versus temperature for select Zn-doped $La_{2-x}Sr_xCuO_4$ samples. Solid lines and dotted lines represent measurements in zero field and 18 T, respectively. Inset shows enlarged view of the x = 0.15 sample in 18 T. Image taken from [14] with copyright permission shown in the Appendix.

than perpendicular [15]. This is because perpendicular fields create vortices in the $CuO_2$ planes that destroy superconductivity more effectively. Thus, we observe different behaviours in our nuclear magnetic resonance (NMR) measurements depending on the external field orientation.

## 1.4 Motivation

Although copper oxide high temperature superconductivity has been discovered over three decades ago, the mechanism inducing perfect conductivity and diamagnetism is still obscure. The isotope effect used to uncover the phonon mediated

superconductivity of conventional superconductors has proven fruitless to demonstrate phonon-mediated electron-electron coupling for high-$T_c$ materials [16, 17]. Thus, physicists have tried to solve this problem by extensively studying the phase diagram of many different compounds. One of the most famous high-$T_c$ cuprates is $La_{2-x}Sr_xCuO_4$ due to its relatively high critical temperature and simple crystal structure.

However, even with its simple crystal structure, many questions still remain about its phase diagram, such as the existence of the pseudogap and charge order. Although $La_{1.6-x}Nd_{0.4}Sr_xCuO_4$ was found to exhibit charge order using neutron and x-ray scattering experiments over two decades ago [9, 10], $La_{2-x}Sr_xCuO_4$'s charge order remained very controversial. One explanation was that Nd-substituted $La_{2-x}Sr_xCuO_4$ undergoes a structural phase transition from a LTO to a LTT, which would pin charge order. NMR experiments found nearly identical signatures indicating the presence of charge order in $La_{1.6-x}Nd_{0.4}Sr_xCuO_4$ [18] also in $La_{2-x}Sr_xCuO_4$ [19], such as the disappearance of the $^{63}$Cu signal, called wipeout, and the divergence of relaxation rates, creating dispute amongst the high-$T_c$ community since other experimental techniques were unable to confirm the existence of charge order two decades ago. When charge and spin order sets in, the relaxation becomes so fast that stripe ordered segments of the sample were undetectable with the current technology at the time. Therefore, the $^{63}$Cu signal was found to be progressively wiped out and the spin-lattice relaxation rate enhanced drastically as charge order settled in, corresponding to the charge order temperature ($T_{charge}$). The same signatures for charge order were found in $La_{1.6-x}Nd_{0.4}Sr_xCuO_4$ with

NMR [18], consistent with neutron and x-ray scattering. However, some experimentalists claimed that these signatures found in NMR were not associated with charge order, but were merely spin glass-like behaviour [20, 21]. Hunt et.al claimed that charge order enhanced low frequency spin fluctuations that caused the relaxation rates to diverge precisely as charge order sets in, resulting in a loss of $^{63}$Cu NMR signal, yet others maintained that no charge order was present due to the apparent absence of Bragg peaks in diffraction measurements at the time [18].

With recent technological advancements, x-ray diffraction experiments have finally been able to detect the charge order Bragg peaks of $La_{2-x}Sr_xCuO_4$, proving that the assertion based on the previous NMR experiments were indeed correct [22, 23]. However, the initial work by Hunt et. al did not find a charge order dome centered at a doping of $\sim 1/8$ for $La_{2-x}Sr_xCuO_4$ [18]. Instead, they initially reported that $T_{charge}$ appeared to increase with decreasing doping even for $x < 1/8$, as shown in Fig. 1.7(a), inconsistent with recent x-ray data and other cuprates. Although they managed to correct themselves for $La_{1.6-x}Nd_{0.4}Sr_xCuO_4$ by observing the $^{63}$Cu wipeout inflection point, as shown in Fig. 1.7(b) [18], for $La_{2-x}Sr_xCuO_4$, Hunt et al. did not revisit the low doping region to clarify the interplay between charge order and charge localization.

Due to the increasingly fast relaxation rates of stripe ordered $^{63}$Cu NMR below $T_{charge}$, previous experiments were unable to measure the $^{63}$Cu NMR signal at low temperatures due to the limiting dead time of the equipment, $t_{dead} \sim 8 - 12\mu s$. Fortunately, with recent advancements of NMR spectrometer technologies, the dead time is reduced to $t_{dead} \sim 2.5\mu s$, enabling us to probe faster relaxing nuclear spins. With state of the art equipment, Imai et al. recently found a

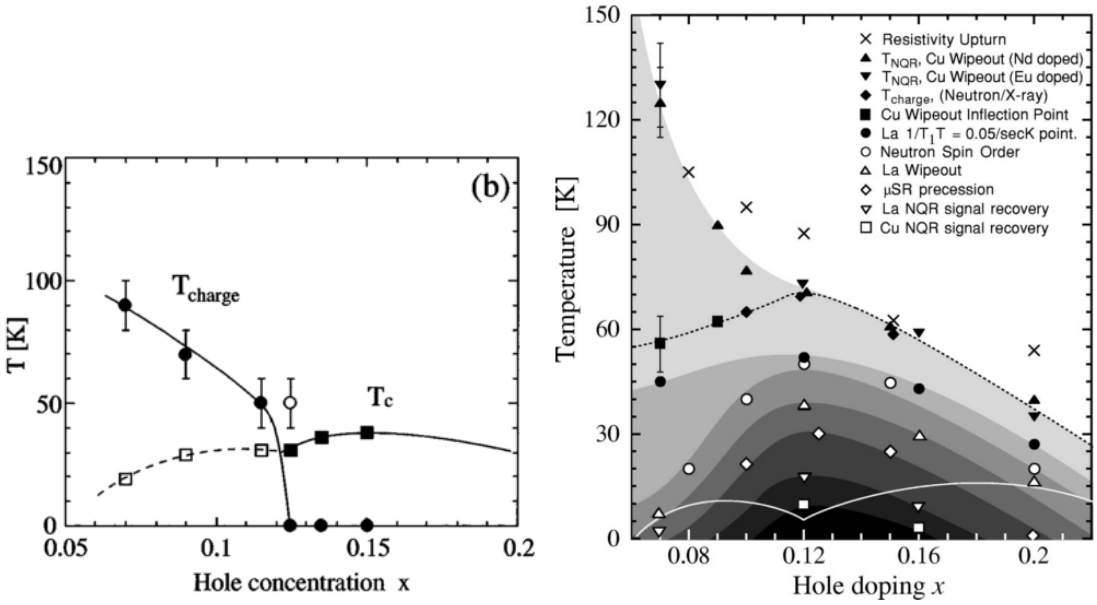


(a) (b)

FIGURE 1.7: (a) Initial phase diagram of $La_{2-x}Sr_xCuO_4$ proposed by Hunt et. al showing that $T_{charge}$ increases below x $\sim$ 1/8. This was obtained before realizing the importance of the inflection point in the $^{63}$Cu signal wipeout for low doping regions. Image taken from [19]. (b) Corrected phase diagram of $La_{1.6-x}Nd_{0.4}Sr_xCuO_4$ proposed by Hunt et. al. The $^{63}$Cu wipeout fraction (▲) has an upturn below x $\sim$ 0.12, while the inflection point (■) correctly reproduces a dome. Image taken from [18] with copyright permission shown in the Appendix.

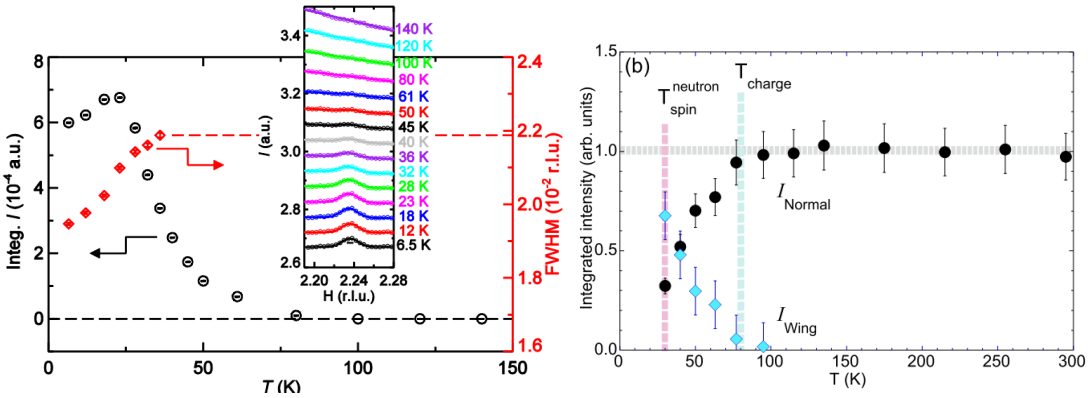


FIGURE 1.8: (left) X-ray scattering experiment on $La_{1.885}Sr_{0.115}CuO_4$ showing the onset of charge order Bragg peaks at $\sim$ 80 K. (right) $^{63}$Cu NMR data on the same $La_{1.885}Sr_{0.115}CuO_4$ crystal demonstrating the transfer of spectral weight from the normal Gaussian-like signal ($I_{Normal}$) to the broad wing-like signal ($I_{Wing}$) starting from $\sim$ 80 K. Images reproduced from [23] and [24] with copyright permission shown in the Appendix.

wing-like signal appearing below $T_{charge}$ for $La_{1.885}Sr_{0.115}CuO_4$, consistent with the emergence of charge order Bragg peaks observed by recent x-ray diffraction measurements conducted on the same sample, as shown in Fig. 1.8 [24].

In this thesis, we show that $^{139}$La NMR is also a good probe for demonstrating the onset of charge order and that results agree well with $^{63}$Cu NMR and x-ray scattering experiments. Although charge order develops in the $CuO_2$ planes, the hyperfine coupling between $^{139}$La nuclei and $^{63}$Cu electrons enables us to indirectly probe these planes. The strong hyperfine interaction between $^{63}$Cu nuclei and their electron spins makes the relaxation rates extremely fast below $\sim$ 20 K in charge ordered domains, preventing signal detection even with current technology. On the other hand, the $^{139}$La nuclei's hyperfine interaction between $^{63}$Cu electron spins is two orders of magnitude lower than $^{63}$Cu nuclei, so that $^{139}$La NMR is still detectable below 20 K.

# Chapter 2

# NMR Basics

NMR has proven to be a very important tool for measuring material properties. Most generally used in chemistry or its varient, Magnetic Resonance Imaging (MRI), in medicine, it has many applications in all fields of science. In physics, NMR is one of the most important tools to probe the local spin dynamics of electrons in solids. The fact that the electrons couple to the nuclei through hyperfine interactions enables us to indirectly probe electron spin dynamics by observing the nuclear spin. In our experiments, we conduct pulsed NMR measurements by sending short pulses with variable frequency that excite the desired nuclei. This chapter will describe the basic theory and experimental setup used for NMR experiments.

## 2.1 Classical Representation

Although atoms behave quantum mechanically, a simplified classical picture is very useful in introducing and visualizing the mechanism behind NMR. Consider a rudimentary nucleus consisting of a charged particle with charge $q$ and mass $m$

moving in a circular loop of radius $r$ at a velocity $\mathbf{V}$. The circulating charge will create a magnetic moment aligned along the rotation axis of the particle, given by [25]:

$$\boldsymbol{\mu} = (q/2mc)/(m\mathbf{V}r) = \gamma\mathbf{J}, \tag{2.1}$$

where $\mathbf{J}$ is the angular momentum. Thus, the angular momentum is proportional to the magnetic moment with a constant of proportionality, $\gamma$, called the gyromagnetic ratio. The magnetic moment will tend to align towards an external magnetic field, creating a torque in the direction of the field given by $\boldsymbol{\tau} = \boldsymbol{\mu} \times \boldsymbol{H}$. However, since the circulating particle, and nuclei in general, have angular momentum, the loop will precess about the external field. Additionally, lattice effects such as magnons and phonons will cause dissipation in the motion of the magnetic moment and given enough time, the moment will align parallel to the external magnetic field. Equating the torque to the rate of change of angular momentum and using Eq. 2.1, we get the equation of motion for the magnetic moment,

$$\frac{d\boldsymbol{\mu}}{dt} = \boldsymbol{\mu} \times (\gamma \boldsymbol{H}), \tag{2.2}$$

showing that changes in $\boldsymbol{\mu}$ are perpendicular to both $\boldsymbol{\mu}$ and $\boldsymbol{H}$. We can solve this equation using standard differential equation techniques, but writing it in a rotating reference frame gives simpler insight into the physics of the rotating moment. In a frame of reference rotating at a frequency $\boldsymbol{\Omega}$, Eq. 2.2 may be

written as:

$$\frac{d\boldsymbol{\mu}}{dt} = \boldsymbol{\mu} \times (\gamma \boldsymbol{H} + \boldsymbol{\Omega}) \,. \tag{2.3}$$

We can see that the rotated frame equation of motion is the same as the lab frame, with an effective field, $\boldsymbol{H_e} = \boldsymbol{H} + \frac{\boldsymbol{\Omega}}{\gamma}$. Requiring that the external field be along the z-axis, $\boldsymbol{H} = H_0 \boldsymbol{z}$, and the resonance frequency, $\boldsymbol{\Omega} = -\gamma H_0 \boldsymbol{z}$, we get $d\boldsymbol{\mu}/dt = 0$ and therefore $\mu$ remains constant in time in the rotational reference frame. $\boldsymbol{\Omega}$ is referred to as the Larmor frequency and is the frequency at which the moment precesses around the external magnetic field.

## 2.2 Quantum Mechanical Representation

A quantum mechanical representation yields a more accurate description of NMR, albeit not as easily pictured. Ignoring any interactions, the nuclei of a solid will have degenerate energy levels associated with their spin. There are many interactions that will lift this degeneracy, but the simplest one is an external magnetic field interacting with the magnetic moment of a nucleus, called the Zeeman interaction. The Hamiltonian for this interaction is given by:

$$\mathcal{H}_{Zeeman} = -\boldsymbol{\mu} \cdot \boldsymbol{H} = -\gamma \hbar H_0 I_z, \tag{2.4}$$

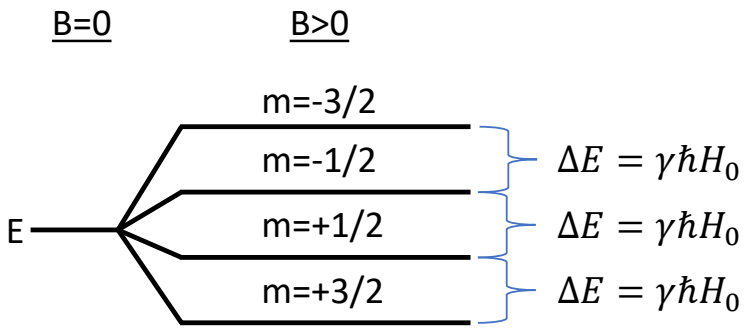


FIGURE 2.1: Energy level diagram for $I = 3/2$, showing that the energy levels are split when a magnetic field is applied.

where $\boldsymbol{J} = \hbar\boldsymbol{I}$ and $\boldsymbol{H} = H_0\boldsymbol{z}$. The eigenvalues are then:

$$E = -\gamma\hbar H_0 m \qquad m = I, I-1, \ldots, -I \tag{2.5}$$

If we consider Cu, which has $I = 3/2$, an external magnetic field will lift the degeneracy into four different energy levels, as shown in Fig. 2.1. We can excite Cu spins lying in low energy states into higher energies by applying an alternating magnetic field perpendicular to the external field at frequency $\omega$ satisfying $\hbar\omega = \Delta E$. These high energy states will interact with the lattice and will therefore dissipate their extra energy to relax back to the low energy states, producing a voltage that can be measured, as explained in the next section.

The full Hamiltonian of the nuclei within a solid is given by:

$$\mathcal{H} = \mathcal{H}_{Zeeman} + \mathcal{H}_{e-n} + \mathcal{H}_Q + \mathcal{H}_{n-n}, \tag{2.6}$$

where $\mathcal{H}_{e-n}$ is the Hamiltonian representing the interaction energy between electrons and nuclei, $\mathcal{H}_Q$ represents the quadrupolar contribution to the energy and $\mathcal{H}_{n-n}$ corresponds to the energy of the interaction between nuclei. We shall not explore each term in the Hamiltonian, but the quadrupolar term will be discussed below as it directly pertains to our measurements.

## 2.3 Quadrupolar Interactions

Quadrupole effects result from the interaction between the nucleus and the surrounding electric field gradient (EFG). When the nucleus is nonspherical ($I > 1/2$), it will have a different energy depending on its orientation in the EFG, as shown in Fig. 2.2. Since the nucleus is electrically positive, its orientation is more energetically favourable when it is closer to negative charges. Therefore, any change in the structure of the lattice will modify the EFG and alter the quadrupole interactions. However, a spherical nucleus will not experience quadrupole effects due to its rotational symmetry, so that nuclei with spin $I \leq 1/2$ do not experience quadrupolar interactions.

The Hamiltonian for quadrupole interactions is given by [26]:

$$\mathcal{H}_Q = \frac{eQV_{ZZ}}{4I(2I-1)}\left[3I_Z^2 - I(I+1) + \frac{1}{2}\eta\left(I_+^2 + I_-^2\right)\right], \tag{2.7}$$

where $Q$ is the quadrupole moment, $V_{ZZ} = \frac{\delta^2 V}{\delta Z^2}$ is the $ZZ$ component of the EFG tensor and $\eta = \frac{V_{XX} - V_{YY}}{V_{ZZ}}$ is the asymmetry parameter describing the asymmetry in

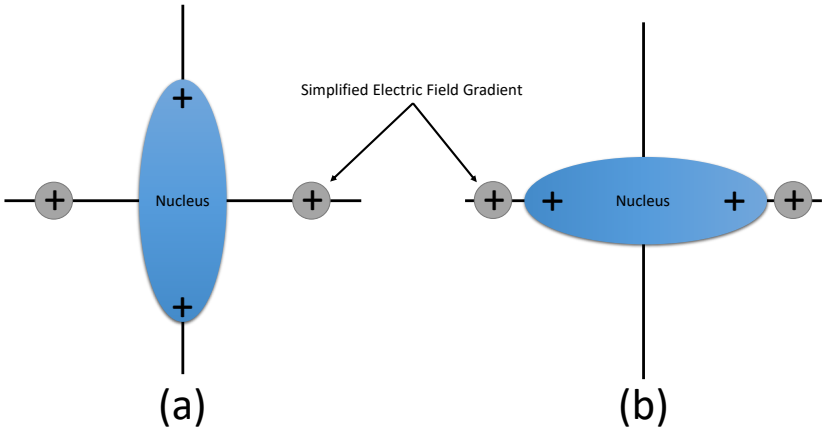


FIGURE 2.2: Different nucleus orientations with respect to the EFG. Orientation (a) is more energetically favourable than (b) since the positive charges are further away from each other.

the EFG. For simplicity, we chose the main principal axes of the symmetric tensor so that $V_{\alpha\beta} = 0$ for $\alpha \neq \beta$. Note that $Z$ is not the same as $z$ for the Zeeman interaction. In this case, $X$, $Y$, and $Z$ are the main principal axes of the EFG tensor $V_{ij}$, with $V_{ZZ}$ being the largest component. $\mathcal{H}_Q$ can be easily diagonalized for the case where $\eta = 0$ to obtain its energy eigenvalues. Nonetheless, for $\eta \neq 0$, closed form solutions have only been obtained for $I = 1$ and $I = 3/2$. Second order perturbation theory and numerical calculations can be used for other spins.

The quadrupolar interaction behaves similarly to the Zeeman interaction by splitting energy level degeneracies. Thus, for $I > 1/2$, we can perform experiments in zero magnetic field called nuclear quadrupole resonance (NQR).

## 2.4 NMR Experiments

In order to probe the energy level splitting created by the external magnetic field ($B_{ext}$) we send a radio frequency (RF) pulse in a coil surrounding the sample perpendicular to the external field. In the rotating reference frame, the moments merely experience a field $B_1$ in the x-direction and will therefore tilt in the y-direction. $B_1$ is applied for a period of time, called $t_{90}$, until the spins have rotated 90° and point in the y-direction. For nuclear spin I = 1/2, $t_{90}$ is given by:

$$\gamma_n B_1 t_{90} = \omega t_{90} = \frac{\pi}{2}. \tag{2.8}$$

When $B_1$ is turned off, the nuclear spins precess about the xy-plane, and according to Faraday's law, a voltage signal, called the Free Induction Decay (FID), can be measured through the same coil used to input the RF pulse. The decay comes from the fact that spins return to equilibrium after a period of time.

FID signals can give a lot of information about the nuclear spins, but they are not ideal since they are affected by field inhomogeneities and contain ringdown of the circuit caused by the RF pulse persisting while the signal is measured, as shown in Fig. 2.3. An improved method of obtaining a measurement is called a spin echo, where the spins are rotated by 180° at a time $\tau$ after the 90° pulse, as schematically shown in Fig. 2.4.

Spin echoes eliminate ringdown effects caused by the high voltage RF pulse lingering due to the finite Q value of the RLC circuit. In regular FID, this persisting

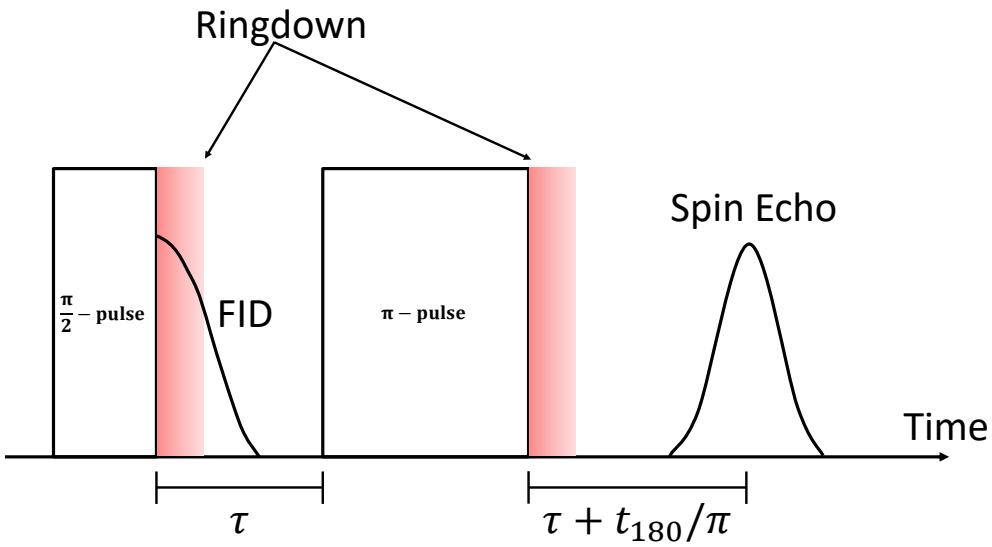


FIGURE 2.3: Spin echo sequence used in our NMR experiments. Ringdown persists for a period of time after each pulse. The FID contains some ringdown, while the spin echo, recorded a time $\tau$ after the $\pi$-pulse, does not.

voltage will be added to the measured FID signal since it is recorded directly after the 90° pulse, rendering a portion of it useless. However, as shown in Fig. 2.3, the spin echo can completely eliminate ringdown since it is recorded a time $\tau$ after the 180° pulse.

Another useful technique for eliminating ringdown is called phase cycling. This is done by carefully choosing the phase of the $\frac{\pi}{2}$-pulse and $\pi$-pulse to destructively add ringdown and constructively add the spin echo signal.

Additionally, spin echo measurements cancel dephasing effects caused by inhomogeneities in magnetic fields, as described in Fig. 2.4. Certain spins precess faster or slower depending on the local field, so that rotating them by 180° minimizes the effect.

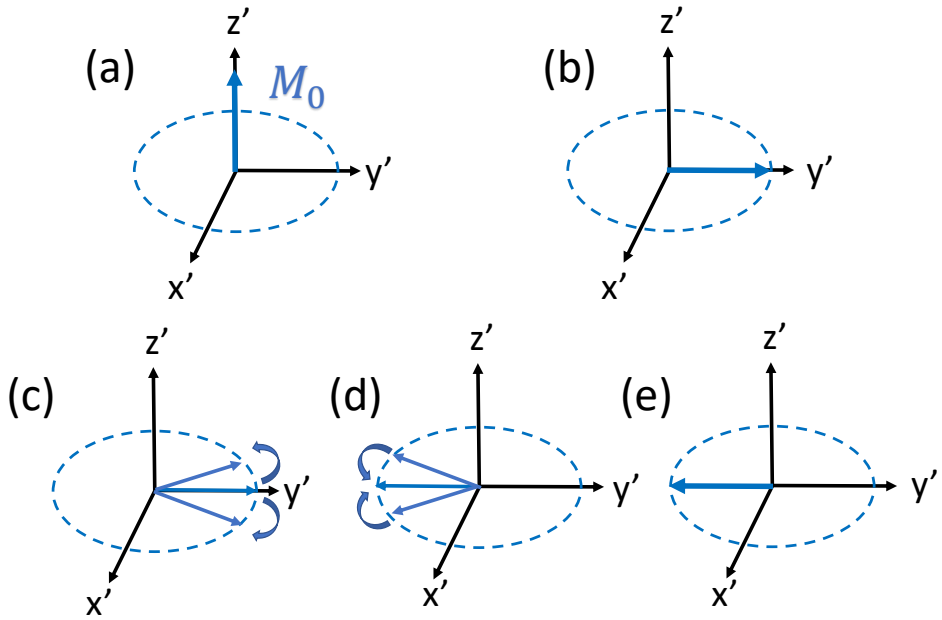


FIGURE 2.4: Real space depiction of spins inside a sample during a spin echo measurement in a rotating reference frame. (a) At t = 0, the net magnetization ($M_0$) lies along the external magnetic field. (b) After a $\frac{\pi}{2}$-pulse, $M_0$ lies along the y' direction. (c) Once $B_1$ is turned off, inhomogeneities in $B_{ext}$ cause spins to have different precessions creating dephasing. (d) A $\pi$-pulse flips the spins along -y'. (e) Finally, the external field inhomogeneities correct the different precession speeds. The spins adding up towards the -y' direction and spreading out again creates the spin echo signal.

## 2.5 Sample Preparation and Experimental Setup

The three crystals were prepared at Tohoku University by M. Fujita and K. M. Suzuki using the traveling solvent floating zone method. Due to the crystal axes not being perfectly aligned with the sample surface for 10% and 13%, we had to rotate the crystal in the probe by machining 1.5cm $\times$ 0.5cm $\times$ 0.5cm plexiglass with the proper rotation angles for each crystal.

The setup used for our NMR experiments is shown in Fig. 2.5. The computer uses a program called TNMR to input the sequence parameters and receive the final digitized signal from the spectrometer. The frequency generator of the spectrometer is employed to create the pulse sequence, that is then amplified by around 60 dB by the power amplifier. The signal is then fed through a set of back to back diodes, which allow only high voltages since low voltages are prevented from going through the diodes.

The RF pulse then goes to the NMR probe, which consists of an LC circuit and contains the sample of interest enclosed in an inductor. By changing the capacitance of the tuning and matching capacitors, the resonance frequency of the LC circuit is set to the frequency of the RF signal. The tuning capacitor is used to set the resonance, while the matching capacitor matches the impedence of the circuit to 50 $\Omega$. This is done to prevent the high voltage pulses from being reflected back and possibly frying other components in the circuit.

A spin echo signal is then produced by the sample as described earlier and is measured by the solenoid. This signal reaches a quarter wavelength ($\lambda/4$) cable

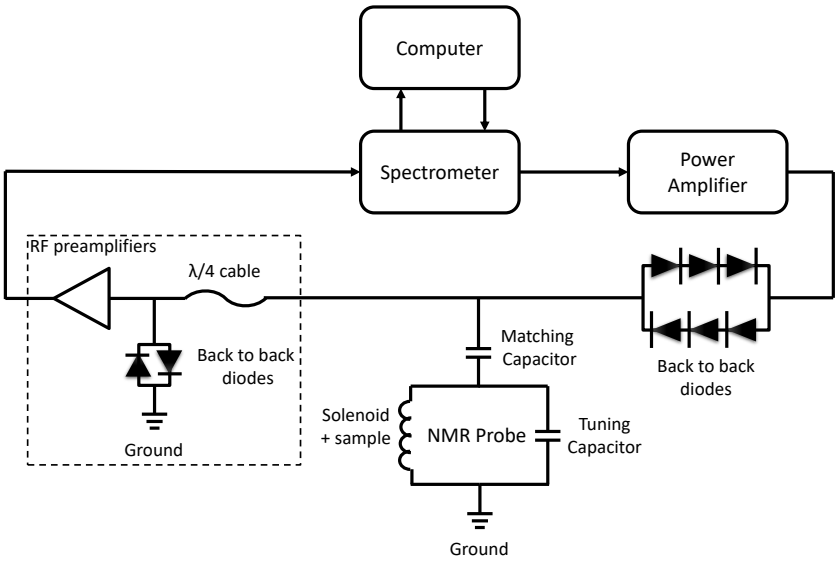


FIGURE 2.5: Diagram of our NMR circuit

that is set to a length of $\sim 45/f_0$, where $f_0$ is the frequency of the RF pulse. This creates a standing wave with a node at the end of the cable for the high voltage RF pulse to short out. A final set of back-to-back diodes shorts any additional high voltages and the signal is sent to a set of preamplifiers before being digitized by the spectrometer.

## 2.6 Spin-Lattice Relaxation Rate Theory

The spin-lattice relaxation rate, $1/T_1$, is one of the most important NMR properties. Simply, the relaxation time, $T_1$, is the duration taken for excited spins to reach thermal equilibrium, i.e. the time taken for tilted spins to align along the external magnetic field. Once the spins are excited using an RF pulse, their energy is dissipated into the lattice by various methods such as interactions with phonons

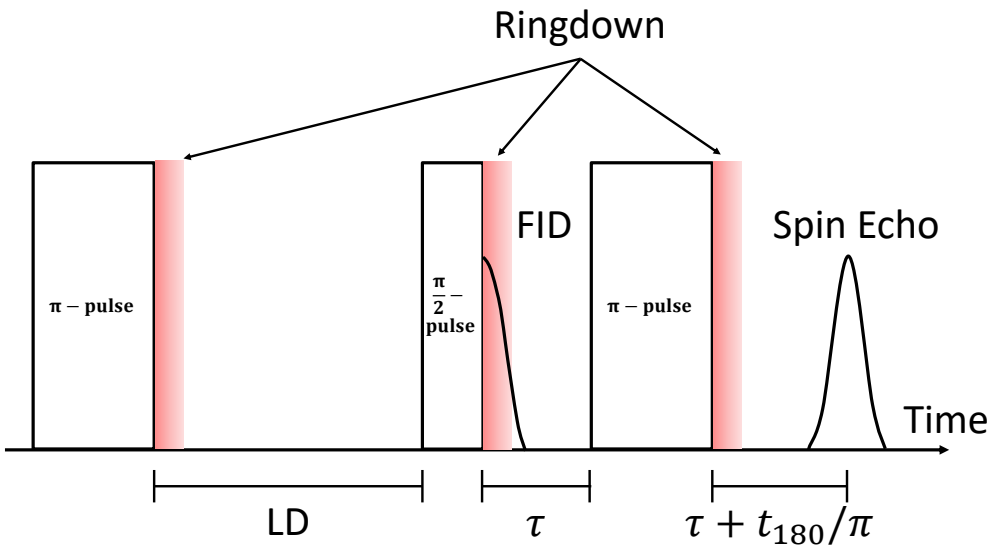


FIGURE 2.6: Sequence used to measure $T_1$.

and magnons. However, the lattice only absorbs low-frequency excitations from the spins, since NMR frequencies are quite low ($\hbar\omega_0/k_B \sim 1mK$).

The pulse sequence used to measure $T_1$ consists of a $\pi$-pulse followed by a regular spin echo, as shown in Fig. 2.6. By varying a time called the long delay (LD) between the $\pi$-pulse and the spin echo sequence, we obtain a relaxation curve that can be fit to appropriate relaxation functions to obtain $1/T_1$. For example, when LD $= 0$, the spins point opposite to the external magnetic field, therefore the spin echo signal is the opposite sign of the LD $\to \infty$ case, where spins have relaxed back to the external field.

To obtain a theoretical expression for $1/T_1$, we perturbatively solve the Hamiltonian $\mathcal{H} = \mathcal{H}_0 + \mathcal{H}_1$, where $\mathcal{H}_0 = H_N + H_{el}$ consists of the Hamiltonian of the bare nucleus and the Hamiltonian of its interaction with electrons. $\mathcal{H}_1$ is the perturbed

Hamiltonian comprising the hyperfine interaction [27]:

$$\mathcal{H}_1 = A\mathbf{I} \cdot \mathbf{S}, \tag{2.9}$$

where A is the hyperfine coupling constant, **S** is the spin of the electron interacting with the nucleus of spin **I**. For simplicity, we assumed A is isotropic. Finding the probability that an initial state $|m_I, n\rangle$ is in the state $|m'_I, n'\rangle$ a time t' later, relating it to the relaxation rate and assuming spin 1/2, we obtain:

$$\frac{1}{T_1} = \frac{A^2}{2\hbar^2} \int_{-\infty}^{\infty} dt \left\langle S^-(t)S^+(0) \right\rangle \exp(i\omega_0 t). \tag{2.10}$$

$\langle S^-(t)S^+(0)\rangle$ represents the thermal average of the electron spin-spin correlation function. The spin ladder operators can be written in terms of their Fourier transform as:

$$S_q^- = \int \exp\left(iq \cdot r\right) S^- dr. \tag{2.11}$$

Using the fluctuation-dissipation theorem, we can rewrite the electron spin-spin correlation function in terms of the imaginary part of the dynamical electron spin-spin susceptibility, $\chi''$, in the low frequency limit [28]:

$$\frac{1}{2} \int_{-\infty}^{\infty} dt \left\langle S_q^+(t)S_q^-(0) \right\rangle \exp\left(i\omega_0 t\right) = \frac{2k_B T}{\omega} \chi''_{\perp}(\mathbf{q}, \omega), \tag{2.12}$$

where $\chi''_{\perp}$ is the spin-spin susceptibility perpendicular to the applied field. Finally, combining Eq. 2.10 with Eq. 2.12, we obtain:

$$\frac{1}{T_1} = \gamma_n^2 A^2 k_B T \sum_{\mathbf{q}} \frac{\chi''_{\perp}(\mathbf{q}, \omega_0)}{\omega_0}. \tag{2.13}$$

Hence, dividing Eq. 2.13 by T, we deduce that $1/T_1T$ simply measures the low frequency spin fluctuations of the observed nuclei perpendicular to the external field.

Another useful way to express $1/T_1$ is in terms of the correlation time, $\tau_c$. Using the field operator $\mathbf{B} = A\mathbf{S}$, assuming that fluctuations in the local field are isotropic and that the correlation function relaxes exponentially, we obtain the simple expression known as the Bloembergen-Purcell-Pound (BPP) result [25]:

$$\frac{1}{T_1} = 2\gamma_n^2 \frac{b_0^2}{3} \frac{\tau_c}{1 + \omega_0^2 \tau_0^2}, \tag{2.14}$$

where $b_0^2$ is the magnitude of the local field. Thus, we expect $1/T_1$ to be a maximum when $\tau_c^{-1} = \omega_0$. Eq. 2.14 will be useful when describing the behaviour of $1/T_1$ versus temperature.

## 2.7 Behaviour of $1/T_1$

Observing the temperature dependence of the spin-lattice relaxation rate is crucial in determining the spin dynamics of a system. Many different processes can cause

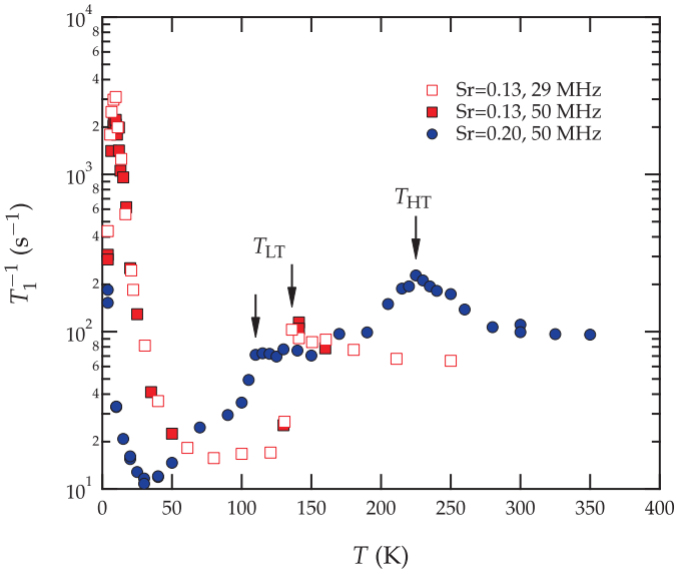


FIGURE 2.7: Enhancement of $^{139}$La NMR $1/T_1$ for $La_{1.8-x}Eu_{0.2}Sr_xCuO_4$ shows both structural phase transitions, $T_{HT}$ and $T_{LT}$, as well as the spin ordering at low temperatures. Graph taken from [29] with copyright permission shown in the Appendix.

$1/T_1$ to increase or decrease, so we shall describe a few relevant examples in this section.

The structural phase transition from the HTT to the LTO phase of $La_{2-x}Sr_xCuO_4$ causes phonon mode softening, meaning that phonon frequencies decrease down to nearly zero. Since NMR is a low frequency probe, the frequency of phonon modes will approach the NMR resonance frequency and $1/T_1$ will increase through the structural phase transition, as shown in Fig. 2.7 for the two structural phase transitions of $La_{1.8-x}Eu_{0.2}Sr_xCuO_4$. $T_{HT}$ is the high temperature structural phase transition from the HTT to the LTO phase, while $T_{LT}$ is the low temperature transition from the LTO to the LTT phase.

Another scenario for $1/T_1$ to increase is when the sample is entering a magnetically ordered state. At higher temperatures, spins will fluctuate at much higher frequencies than the NMR frequency, $\omega > \omega_0$. Lowering the temperature near the ordered state makes the spin fluctuations slow down, until $\omega = \omega_0$, causing $1/T_1$ to reach a maximum, according to Eq. 2.14. Additional lowering of the temperature makes the spins fluctuate at even lower frequencies, meaning that $1/T_1$ decreases when $\omega < \omega_0$. Since $\omega_0$ is very low for NMR, we associate the temperature at which $1/T_1$ is peaked to the spin freezing temperature. The behaviour described above is observed in many different spin ordering states, such as spin density wave, spin glass, and Néel states and is manifested in the spin ordered state of $La_{1.8-x}Eu_{0.2}Sr_xCuO_4$ in Fig. 2.7 below 50 K.

Finally, an important method in determining the type of superconductivity of a material is by monitoring its relaxation rate near the superconducting critical temperature. Upon entering the superconducting state, an energy gap is formed at the Fermi energy between the ground state and the first excited state. For conventional superconductors, the gap is isotropic and is referred to as s-wave, analogous to electron orbitals. For s-waves, the density of states near the Fermi energy diverges, as shown in Fig. 2.8. However, for higher order gap symmetries such as d-wave and p-wave, nodes form in the gap. Thus, since $1/T_1$ indirectly measures electron spin fluctuations near the Fermi level, the symmetry of the gap is reflected in spin-lattice relaxation measurements, as shown in Fig. 2.9. The divergence of the density of states for s-wave superconductors causes a peak in $1/T_1$, called the Hebel-Slichter coherence peak [30].

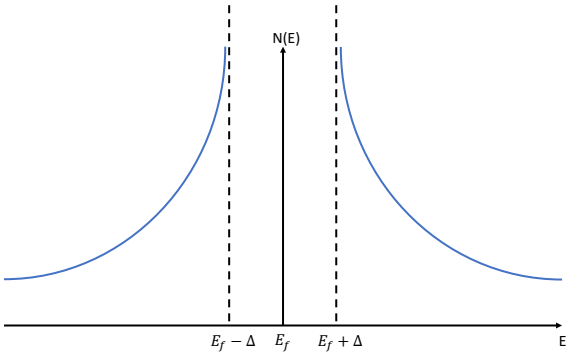


FIGURE 2.8: Schematic diagram of the density of states for s-wave superconductors near the Fermi level.

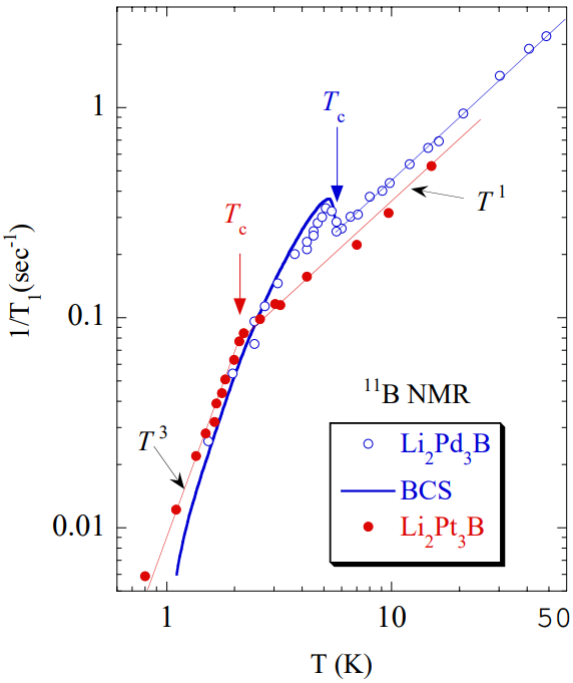


FIGURE 2.9: Comparison of $^{11}$B NMR $1/T_1$ measurements between conventional, $Li_2Pd_3B$, versus unconventional, $Li_2Pt_3B$, superconductors. A Hebel-Slichter coherence peak is only observed for $Li_2Pd_3B$. Graph taken from [31] with copyright permission shown in the Appendix.

# Chapter 3

# $^{139}$La NMR Measurements

As discussed in Sec. 1, $^{139}$La NMR is a good indirect probe of charge order due to its modest hyperfine interaction between $^{139}$La nuclear spins and $^{63}$Cu electron spins. Previous $^{63}$Cu NMR work on $La_{1.885}Sr_{0.115}CuO_4$ found that a different wing-like signal appeared below $T_{charge} \sim 80$ K with a much faster relaxation rate than the normal Gaussian-like signal. Therefore, we expect regions of the sample to behave like a stripe ordered phase with fast relaxation, while others will behave like a superconductor with slow relaxation. We introduced a double component fit for the relaxation curves of $^{139}$La NMR as discussed below, resulting in good agreement with $^{63}$Cu NMR and x-ray scattering experiments. We recently published a paper on $La_{1.885}Sr_{0.115}CuO_4$ [32], but I wasn't the main author so I will give a brief discussion of the results in the next section. The section after that will detail our x = 0.13 and 0.10 measurements conducted entirely by myself.

## 3.1 $La_{2-x}Sr_xCuO_4$ x=0.115

There are three main properties of $^{139}$La NMR that demonstrate the onset of charge order, the half width at half maximum ($\Delta$f) of the lineshape, the spin-lattice relaxation rate and the fraction of the sample that has fast ($I_{fast}$) and slow ($I_{slow}$) relaxation.

### 3.1.1 11.5% Lineshapes

We measured the $^{139}$La NMR $I_z = +1/2$ to -1/2 central transition in magnetic fields of 9 T parallel to the c-axis on an $La_{1.885}Sr_{0.115}CuO_4$ single crystal, as summarized with select lineshapes in Fig. 3.1(a). Solid lines represent lineshapes symmetric enough to fit to a Gaussian, while dotted lines are guides for the eye. Above 220 K, the $CuO_6$ octahedra point along the c-axis, parallel with $B_{ext}$. Thus, there is no quadrupole shift and the lineshape is narrow enough to do a Fast Fourier Transform (FFT). The lineshapes are asymmetric due to the disorder caused by $Sr^{2+}$ substitution. When going through the structural phase transition, the $CuO_6$ octahedra tilt along the diagonal of the squares formed by Cu atoms, creating a second order quadrupole shift that lowers the resonance frequency ($f_0$), as shown in Fig. 3.2(a). Due to a distribution in rotation angle and nuclear quadrupole frequency, the lineshape drastically broadens through $T_{HTT-LTO} \sim 250$ K, as demonstrated by the drastic increase of $\Delta$f in Fig. 3.2(b). Below 180 K, we found that the lineshapes are almost perfect Gaussians, so we fit them to Gaussians for a better accuracy of $f_0$ and $\Delta$f.

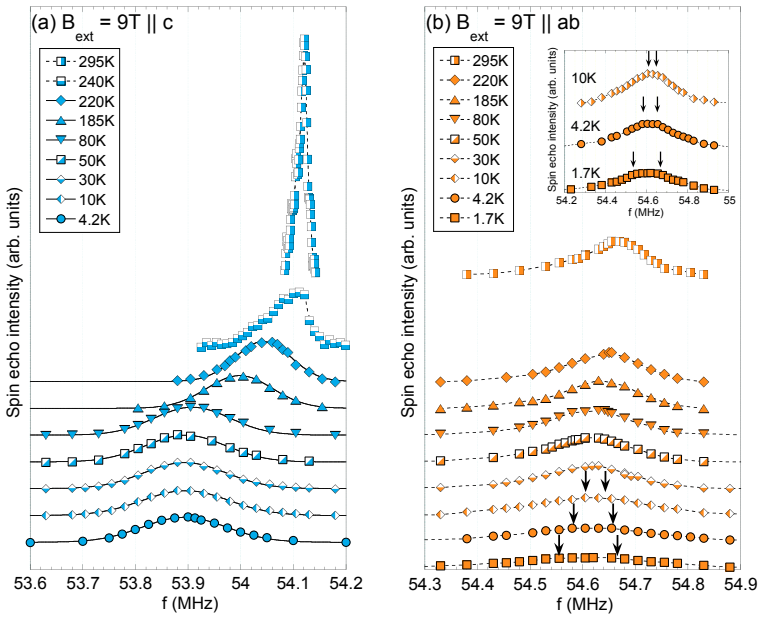


FIGURE 3.1: $La_{1.885}Sr_{0.115}CuO_4$ lineshapes for select temperatures for an external field of 9 T parallel to (a) the c-axis and (b) the Cu-O-Cu bond direction.

When $B_{ext}$ || ab, the second order quadrupole shift, $\Delta\nu_Q^2$, is finite. Therefore, since there is a distribution in $\nu_Q$, the lineshapes are broad even at 295 K, as shown in Fig. 3.1(b) and Fig. 3.2(b). The linewidth is further enhanced through $T_{HTT-LTO}$, until it reaches a plateau at $\sim$ 150 K for both $B_{ext}$ || c and ab. Note that for $B_{ext}$ || ab, the lineshapes are always asymmetric, meaning that a Gaussian fit cannot estimate the width as accurately as for $B_{ext}$ || c.

The linewidth slightly increases for both field orientations below $T_{charge} \sim 80$ K, the same charge order temperature as obtained in $^{63}$Cu NMR and x-ray experiments [23, 24]. However, we confirmed that in 4.5 T, the apparent line broadening is suppressed by a factor of $\sim$ 2, meaning that the broadening is of paramagnetic origin and not quadrupole effects. Therefore, broadening near $\sim$ 80 K is due to

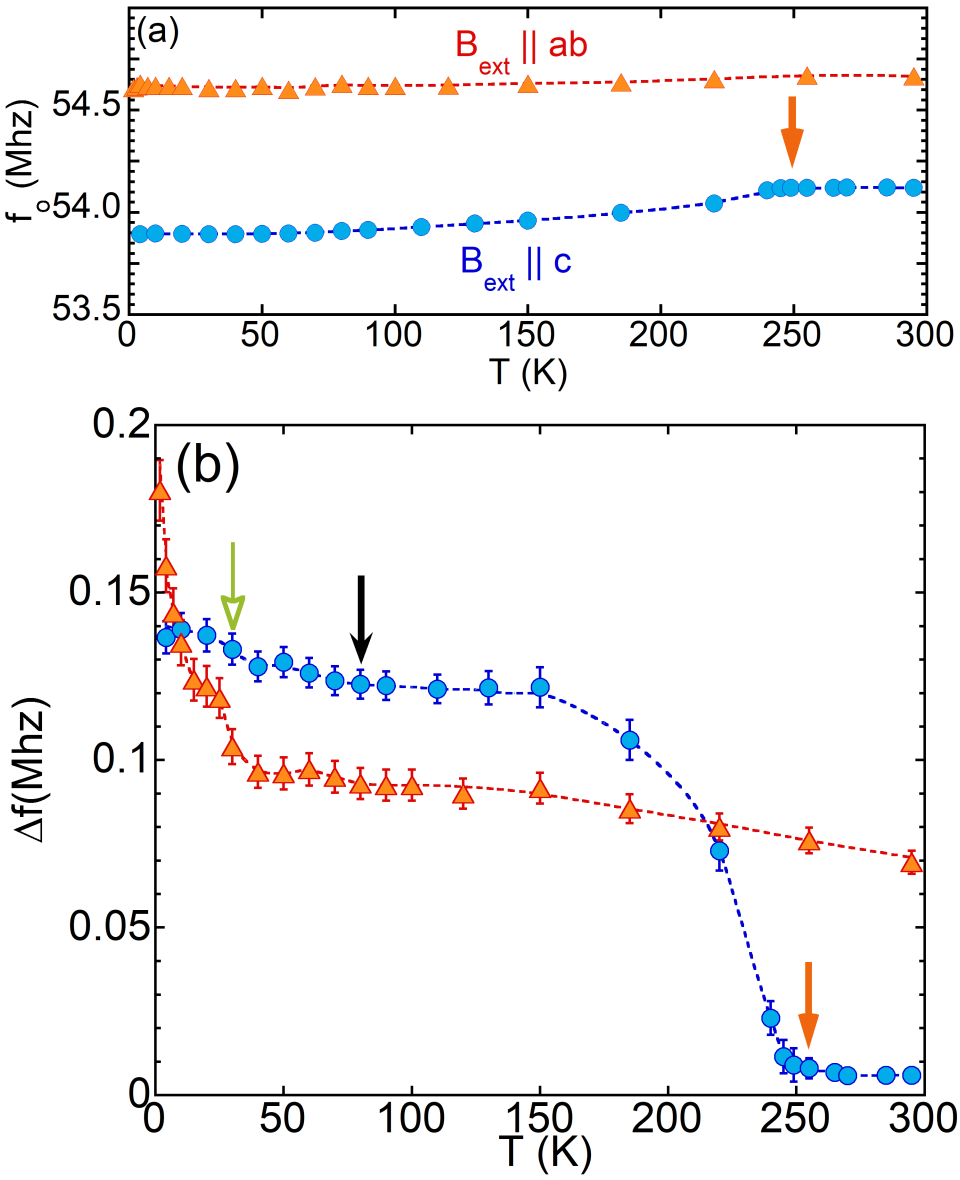


FIGURE 3.2: (a) Temperature dependence of $f_0$. The orange arrow denotes the structural phase transition, $T_{HTT-LTO} \sim 250$ K. (b) $\Delta$f versus temperature. The black and green arrows denote the charge ordering temperature, $T_{charge} \sim 80$ K, and the spin ordering at the neutron scattering timescale, $T_{spin}^{Neutron} \sim 30$ K. Figure reproduced from [32] with copyright permission shown in the Appendix.

spin effects. Δf plateaus once again and finally broadens below $T_{spin}^{Neutron} \sim 30$ K, when antiferromagnetic spin correlations are enhanced before spin freezing sets in.

### 3.1.2 $1/T_1$ Measurements

We measured $1/T_1$ at the central peak of $^{139}$La sites in order to examine the effect of spin and charge order on $^{63}$Cu spins. Due to the better signal to noise ratio when $B_{ext} \parallel c$, we used $1/T_1$ of this configuration to split the recovery curves into two components, as described in the next section. A comparison of the standard stretched fit, which captures the average relaxation rate of the sample, versus the double component fit, which splits the relaxation rate into two components, of the relaxation curves is shown in Fig. 3.3. Notice that the relaxation curve at 30 K crosses that of 185 K, meaning that both faster and slower relaxing components are present at 30 K. Our finding that $^{139}$La spins contain two drastically different relaxation rates below $T_{charge}$ substantiates the appearance of the $^{63}$Cu NMR wing-like signal and validates the use of a double component fit.

The temperature dependences of $1/T_1$ is shown in Fig. 3.4(a). Notice that below $T_{charge}$, the average $1/T_1$ obtained from the stretched fit is split into a fast ($1/T_1^{fast}$) and slow ($1/T_1^{slow}$) relaxation rate when using a double component fit. $1/T_1^{fast}$ behaves like the average relaxation rate, increasing with decreasing temperature until it reaches a maximum at the spin ordering temperature $T_{spin} \sim 8$ K. $1/T_1^{slow}$, however, still decreases below $T_{charge}$, behaving like the optimally superconducting $La_{1.85}Sr_{0.15}CuO_4$ above its $T_c = 38$ K [33].

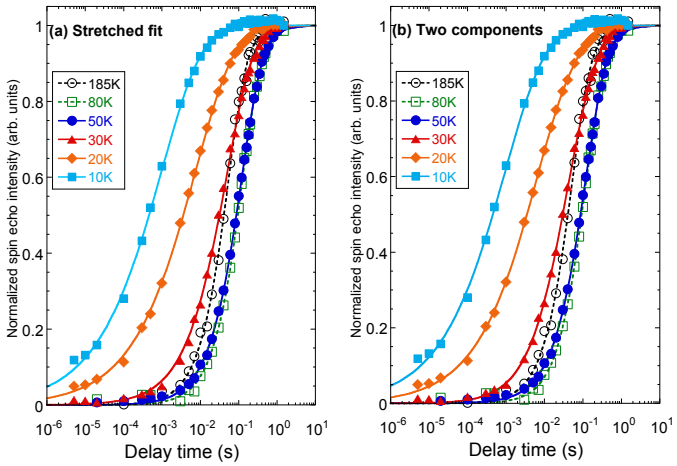


FIGURE 3.3: Comparison of both the stretched (a) and double component (b) fits for the same relaxation curves. Both fit the data very well, but give drastically different information, as explained in the text. Figure reproduced from [32] with copyright permission shown in the Appendix

The volume fraction of the sample containing fast and slow relaxation is shown in Fig. 3.4(b). At high temperatures, 100% of the sample is uniquely slowly relaxing. However, below $T_{charge}$, a fast component emerges, in agreement with the appearence of a broad, wing-like $^{63}$Cu NMR signal with fast relaxation. Thus, we concluded that $T_{charge} \sim 80$ K and that $^{139}$La NMR is also a good probe for charge order in the cuprates, since our results agreed with the charge order temperatures obtained from $^{63}$Cu NMR and x-ray scattering experiments.

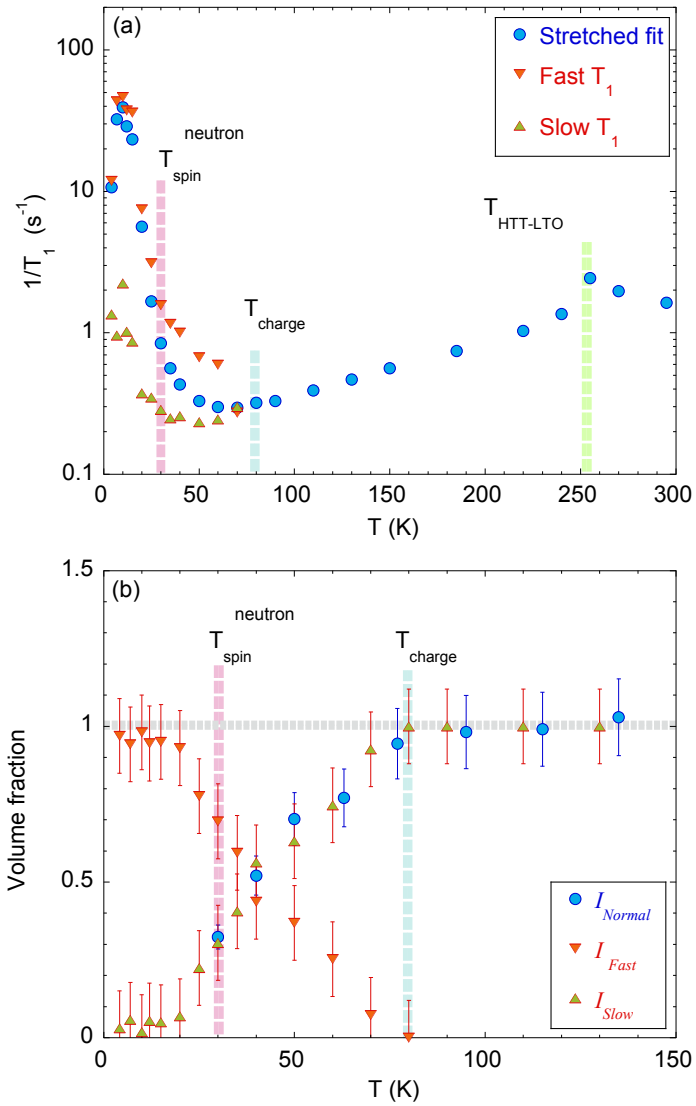


FIGURE 3.4: (a) Temperature dependence of the average $1/T_1$ (filled bullets) obtained from a stretched fit and the fast (downward triangle) and slow (upward triangle) relaxation rates obtained from a double component fit. (b) Volume fraction of fast and slow components versus temperature. $I_{fast}$ decreases from one at $T_{charge}$ down to zero at $\sim$ 20 K. $I_{normal}$ represents the integrated intensity of the normal $^{63}$Cu NMR signal, showing the same behaviour as $I_{fast}$. Figure reproduced from [32] with copyright permission shown in the Appendix

## 3.2 $La_{2-x}Sr_xCuO_4$ 13% and 10% Paper

*Investigation of charge order in $La_{2-x}Sr_xCuO_4$ single crystals using $^{139}La$ NMR*

**A. Arsenault** S. K. Takahashi, T. Imai, K. M. Suzuki, M. Fujita

To be submitted to Physical Review B (2018).

This section focuses on our most recent manuscript of $^{139}$La NMR on $La_{2-x}Sr_xCuO_4$ 13% and 10% single crystals. We compare all three doping concentration measurements and observe the difference in relaxation rate behaviour. By producing the same analysis as in the last section, we were able to map out the charge order dome of the phase diagram and monitor the effect of stripe order on spin dynamics.

**Author Contributions**:

1. *NMR Experiments*: **A. Arsenault**, S. K. Takahashi, T. Imai
2. *Data Analysis*: **A. Arsenault**, T. Imai
3. *Manuscript*: **A. Arsenault**, S. K. Takahashi, T. Imai
4. *Sample Preparation*: K. M. Suzuki, M. Fujita

## 3.3 Abstract

We present comprehensive $^{139}$La NMR lineshape and spin-lattice relaxation rate measurements on single crystal samples of $La_{2-x}Sr_xCuO_4$ for x = 0.13 and 0.10. From the comparison of $^{139}$La NMR data on $La_{1.885}Sr_{0.115}CuO_4$ with the optimal hole concentration of charge order, $T_{charge} = 80\pm10$ K, we identify the $^{139}$La NMR anomalies that manifest themselves at the charge ordering temperature of $T_{charge} = 65\pm10$ K for 13% and $T_{charge} = 65^{+12}_{-10}$ K for 10%. These new NMR data contributed to a charge order dome centered around 11.5%. Based on a two component analysis of the nuclear relaxation curves, we estimate the volume fraction, $I_{fast}$, of the $CuO_2$ planes hosting fast relaxing $^{139}$La sites that are under the influence of enhanced low frequency Cu spin fluctuations triggered by charge order. $I_{fast}$ is not 100% immediately below $T_{charge}$, but instead grows progressively below $T_{charge}$.

## 3.4 Introduction

Since the discovery of high-$T_c$ cuprates more than three decades ago, many authors attempted to establish the electronic phase diagram to elucidate the mystery behind the mechanism of superconductivity. To this day, there remain many unanswered questions regarding the different phases of high-$T_c$ cuprates, such as the pseudogap and charge density wave order. Luckily, recent advancements in measurement technology have enabled experimentalists to probe new regions of the phase diagram that were not previously possible. For example, many different forms of charge order were discovered in various high-$T_c$ cuprates. Scanning

tunneling microscopy (STM), resonant x-ray scattering (RXS) and angle-resolved photoemission spectroscopy (ARPES) experiments demonstrated that charge order is short-ranged in underdoped samples of $Bi_2Sr_2CaCu_2O_{8-x}$ (Bi-2212) and $Bi_2Sr_{2-x}La_xCuO_{6+\delta}$ (Bi-2201) [34, 35] and in $HgBa_2CuO_{4+\delta}$ in zero field [36]. In (Y,Nd)$Ba_2Cu_3O_{6+x}$ compounds, long-ranged charge order fluctuations were found to be incommensurate with a periodicity of $\sim 3.2$ lattice units with resonant soft x-ray scattering [37]. More recently, long-ranged field induced charge order was discovered in Bi-2201 and $YBa_2Cu_3O_y$ with fields $\gtrsim$15 T using nuclear magnetic resonance (NMR) [38, 39].

$La_{2-x}Sr_xCuO_4$ is one of the simplest high-$T_c$ cuprates in terms of crystal structure, but it was in $Nd^{3+}$ co-doped $La_{2-x}Sr_xCuO_4$ where charge order was initially discovered [12]. Nonetheless, the existence of charge order in $La_{2-x}Sr_xCuO_4$ has been debated for over two decades due to the apparent lack of charge order Bragg peaks. Fortunately, the presence of charge order in $La_{2-x}Sr_xCuO_4$ ($x \sim 1/8$) has finally been firmly established based on observation of charge order Bragg peaks with x-ray scattering experiments [22, 23, 40], nearly two decades after earlier NMR measurements concluded its presence [18, 19].

In this paper, we present comprehensive $^{139}$La NMR measurements on $La_{2-x}Sr_xCuO_4$ single crystals for x = 0.13 and 0.10, and compare the new data with previously published results for x = 0.115 [32]. In the case of x = 0.115, we demonstrated that the spin-lattice relaxation rate ($1/T_1$) at $^{139}$La sites can be split into a fast and slow component below the charge ordering temperature at $T_{charge} \sim 80$ K. Moreover, we showed that a new broad, wing-like $^{63}$Cu NMR signal emerges below charge order with a much faster relaxation rate than the

| Doping | $T_c$ | $T_{HTT-LTO}$ | $T_{charge}$ | $T_{spin}^{Neutron}$ |
|---|---|---|---|---|
| 0.13 | 35 K | 245 K | 65±10 K | 25±5 K |
| 0.115 | 30 K | 255 K | 80±10 K | 30±5 K |
| 0.10 | 27 K | >295 K | $65^{+12}_{-10}$ K | 25±5 K |

TABLE 3.1: Summary table of $La_{2-x}Sr_xCuO_4$ results obtained in this paper and in Ref. [32] for x = 0.13, 0.115 and 0.10.

normal, superconductor-like signal [24]. Due to the exceptionally fast relaxation of the wing-like signal, it can only be detected with extremely short NMR pulse separation time $\tau \sim 2$ $\mu$s, which explains why it has only been recently discovered. Since the spectral weight of wing-like $^{63}$Cu NMR signal agrees with that of faster $^{139}$La $1/T_1$ in $La_{1.885}Sr_{0.115}CuO_4$, we can therefore probe the charge ordered regions with enhanced spin dynamics separately and identify the onset of charge order where the $^{139}$La $1/T_1$ splits into two components. We demonstrate that charge order enhances low frequency Cu spin fluctuations, but some segments of $CuO_2$ planes remain unaffected by charge order even far below $T_{charge}$. Following our $La_{1.885}Sr_{0.115}CuO_4$ results, we determined the onset of spin order at the neutron scattering timescale $T_{spin}^{Neutron}$ by identifying the strong enhancement of the linewidth at low temperature when the external field is parallel to the Cu-O-Cu bond direction.

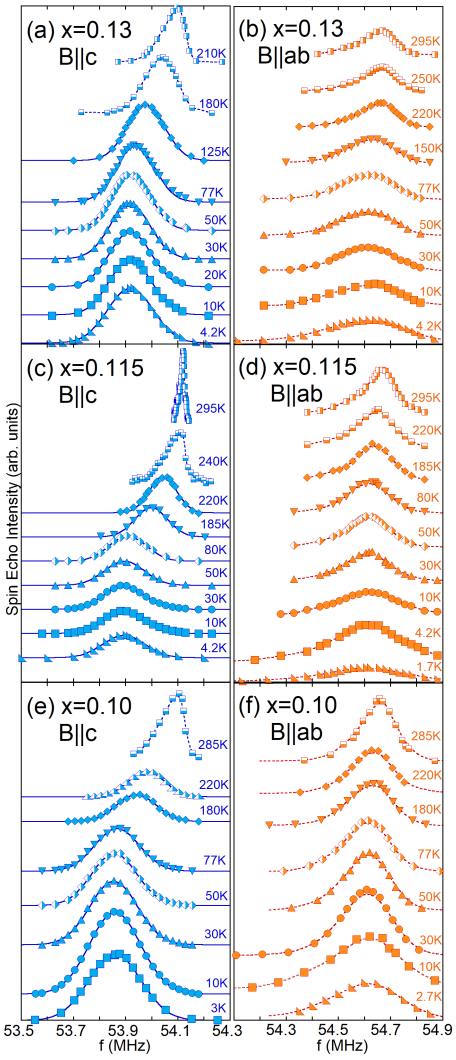


FIGURE 3.5: $^{139}$La NMR lineshapes measured for (a)(b) x = 0.13, (c)(d) x = 0.115, and (e)(f) x = 0.10 in an external field of 9 T parallel to (blue) the c-axis and (orange) the Cu-O-Cu bond direction. Lineshapes are displaced vertically at different temperatures for clarity. At low temperatures for $B_{ext}$ || c, lineshapes are symmetric and can be nicely fitted with a Gaussian, as shown with the solid curves. Dashed curves are guides for the eye through asymmetric lineshapes.

## 3.5 Results and Discussions

### 3.5.1 Sample Growth and Characterization

We grew the single crystals of $La_{2-x}Sr_xCuO_4$ at Tohoku using the traveling solvent floating zone method. We determined the superconducting critical temperature summarized in Table. 3.1 by measuring the magnetic susceptibility using a superconducting quantum interference device (SQUID). We conducted the NMR measurements at McMaster based on standard pulsed NMR techniques. All three dopings measured show different spin fluctuation behaviours at low temperature. We begin by investigating the x = 0.13 region.

### 3.5.2 $^{139}$La NMR Results for x = 0.13

Figs. 3.5(a) and (b) show representative $^{139}$La NMR lineshapes for the $I_z = +1/2$ to $-1/2$ central transition observed for x = 0.13. Fig. 3.5(a) is for an external magnetic field of 9 T applied parallel to the c-axis, while Fig. 3.5(b) is for the external field applied parallel to the Cu-O-Cu bond direction. Lineshapes for $B_{ext}$ || c below 180 K were symmetric enough to be accurately fit to a Gaussian, as shown by the solid curve through the data. Dotted lines are guides for the eye for asymmetric lineshapes at and above 180 K and for $B_{ext}$ || ab. The lineshapes are broader for 13% than 11.5% in Figs. 3.5(c) and (d) and 10% in Figs. 3.5(e) and (f) due to the added disorder from $Sr^{2+}$ substitution and possible misalignment of the crystal by $\sim$ 2°, as discussed in the Appendix. A summary and discussion of the peak frequency and linewidth versus temperature is detailed in the Appendix.

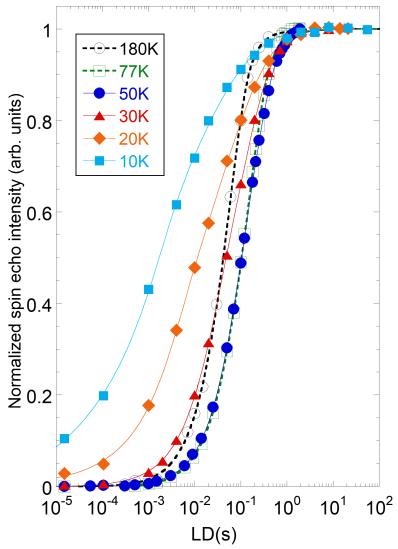


FIGURE 3.6: Spin-lattice relaxation curves for select temperatures. The curves are fit to a double component fit and normalized so that A=$B_1$+$B_2$=1 in Eq. 3.2. The relaxation curves for 11.5% and 10% are similar, so they have not been shown.

To examine the effects of charge ordering on spin fluctuations, we measured the spin-lattice relaxation rate versus temperature. Earlier experiments on $La_{2-x-y}(Nd,Eu)_ySr_xCuO_4$ showed that charge order triggers the enhancement of low frequency spin fluctuations and $1/T_1$ begins to grow below $T_{charge}$ [18]. This enhancement is accompanied by the emergence of a distribution of relaxation rates, because charge order sets in inhomogeneously throughout the sample volume [18, 19]. Analogous distribution of $1/T_1$ was also found to be present in $La_{2-x}Sr_xCuO_4$ [18, 32, 41–43]. Therefore, we must carefully analyze the spin echo recovery curves ($M(t)$) near $T_{charge}$.

We use two different fitting functions to fit the $^{139}$La NMR spin-lattice relaxation curves, one to obtain the average relaxation rate of the sample and the other to split the relaxation rate into a fast and slow component. The average relaxation

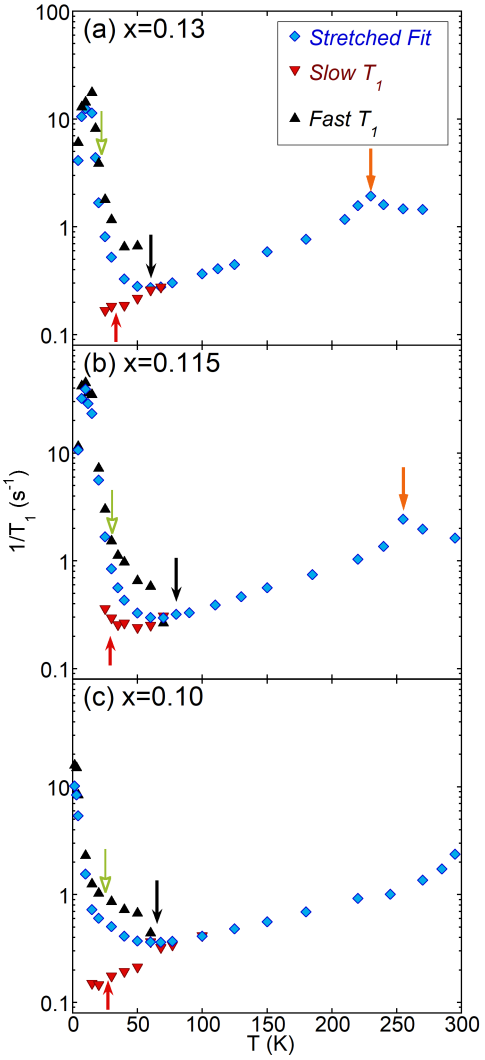


FIGURE 3.7: Downward (upward) triangles represent $1/T_1^{slow}$ ($1/T_1^{fast}$) deduced from the double fit with Eq. 3.2 for (a) x = 0.13, (b) x = 0.115 and (c) x = 0.10 for $B_{ext}||c$. For comparison, we also show the average $1/T_1$ results obtained from the single component stretched fit in blue. The orange arrow marks $T_{HTT-LTO}$, the red arrow marks $T_c$, and the black and green arrows mark the onset of $T_{charge}$ and $T_{spin}^{Neutron}$, respectively. We excluded $1/T_1^{slow}$ when $I_{slow}$ reaches below 20%, since the double component fit fails to capture the relaxation rate of the small volume of the sample containing $1/T_1^{slow}$.

rate is obtained with the standard stretched fit:

$$M(t) = A - B[\Sigma_i p_i \cdot e^{-(q_i t/T_1)^\beta}], \tag{3.1}$$

where A, B and $1/T_1$ are the fitting parameters, and $p_i$ and $q_i$ are coefficients determined theoretically for the $\Delta I_z = \pm 1$ magnetic transition [44, 45]. $\beta$ is a phenomenological stretched fit parameter that deviates from one when there is a distribution of relaxation rates or if quadrupolar relaxation has a non-negligible contribution ($\Delta I_z = \pm 2$). The temperature dependence of $\beta$ is summarized in the Appendix.

Although the single component analysis using Eq. 3.1 suitably fits the recovery data and captures some interesting properties of the system such as spin freezing, key physics has been left out when considering only the average relaxation rate. In fact, close examination of the recovery curves reveals that the curves observed at 10 K, 20 K, and 30 K cross that of 180 K, as seen in Fig. 3.6. This means that at low temperatures, a certain fraction of $^{139}$La nuclear spins in some segments of $CuO_2$ planes actually have slower $1/T_1$ than at 180 K, and the average $1/T_1$ deduced from the fit to Eq. 3.1 completely overlooks this fact. The fast component corresponds to the NMR signal arising from charge ordered segments of $CuO_2$ planes, while the slow component corresponds to the remaining segments uninfluenced by charge order [32]. We therefore split the relaxation rate into a fast ($1/T_1^{fast}$) and slow ($1/T_1^{slow}$) component by fitting relaxation curves with an

additional term to Eq. 3.1:

$$M(t) = A - B_1[\Sigma_i p_i \cdot e^{-(q_i t/T_1^{fast})^{\beta}}] - B_2[\Sigma_i p_i \cdot e^{-(q_i t/T_1^{slow})}]. \tag{3.2}$$

To minimize the number of parameters and get a better fit, we found it sufficient to only add $\beta$ to the fast component, which arises when charge order sets in.

We plot the temperature dependence of the average, fast and slow relaxation rates of x = 0.13 in Fig. 3.7(a) for $B_{ext}$ || c. $1/T_1$ reaches a local maximum at $T_{HTT-LTO} \sim 245$ K, marked by the orange arrow, where the phonon modes soften to the NMR frequency at the structural phase transition temperature, $T_{HTT-LTO}$. The relaxation rate decreases monotonously down to $\sim 65$ K, where it is enhanced by low frequency spin fluctuations caused by the onset of charge order, indicated by the black arrow. This temperature also marks the splitting of the average relaxation rate into a fast and slow component. The average $1/T_1$ reaches a maximum when the spin fluctuations slow down to the NMR frequency at $\sim 10$ K, marking the spin ordering temperature at the NMR timescale. The temperature dependence of $1/T_1^{fast}$ is what one would expect in the vicinity of a magnetic instability; $1/T_1^{fast}$ is enhanced strongly towards the base temperature due to the enhancement of low frequency spin fluctuations.

However, $1/T_1^{slow}$ is persistently slow below $T_{charge}$ down to $\sim 15$ K through the onset of superconductivity marked by the red arrow, unaffected by charge and spin ordering. This indicates that the presence of the sample volume still behaving like a typical d-wave superconductor far from magnetic instabilities, even

though the average relaxation rate obtained from a single component stretched fit completely fails to capture this signature. Due to the limited (<20%) volume fraction containing slow relaxation, the double component fit becomes unstable for $1/T_1^{slow}$ below $\sim$ 15 K. Thus, we omit data points below $\sim$ 15 K for $1/T_1^{slow}$. For 11.5%, we found a strong enhancement of the linewidth corresponding to $T_{spin}^{Neutron}$ at $\sim$ 30 K. Analogously, from the temperature dependence of the linewidth summarized in the Appendix, we deduce that $T_{spin}^{Neutron} \sim$ 25 K for 13%, as marked by the green arrow.

In Fig. 3.8(a), we summarize the temperature dependence of the volume fractions containing fast, $I_{Fast} = B_1/(B_1 + B_2)$, and slow, $I_{Slow} = B_2/(B_1 + B_2)$, relaxation obtained from the double component fit, Eq. 3.2. The volume fractions follow similar behaviour as those of the optimal charge order doping of x = 0.115 in Fig. 3.8(b), with $I_{fast}$ emerging roughly linearly starting at $\sim$ 65 K and increasing to $\sim$ 85% down to $\sim$ 15 K. For x = 0.115, both the emergence of fast $^{139}$La spin-lattice relaxation rate and wing-like $^{63}$Cu NMR signal occur at the same temperature of $T_{charge} \sim$ 80 K, consistent with x-ray experiments [23]. Accordingly, we conclude that $T_{charge} \sim 65\pm10$ K for x = 0.13.

### 3.5.3 x = 0.10

The $^{139}$La NMR lineshapes for the $I_z = +1/2$ to $-1/2$ central transition for x = 0.10 are summarized in Figs. 3.5(e) and (f). A discussion of the resonance frequency and linewidth versus temperature is described in the Appendix.

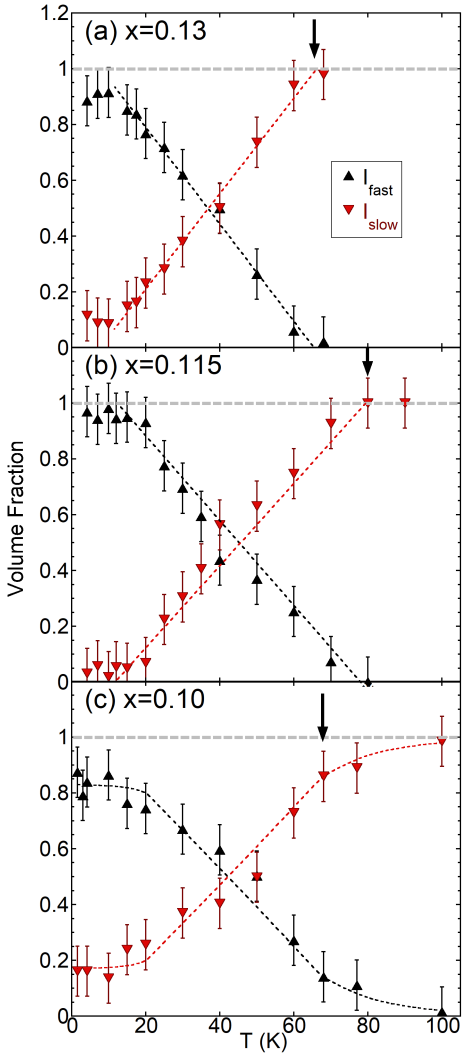


FIGURE 3.8: Volume fraction $I_{slow}$ (downward triangle) and $I_{fast}$ (upward triangle) as a function of temperature. Dashed lines are guides for the eye. (a) x = 0.13. The emergence of $I_{fast}$ marks the onset of charge order at $\sim$ 65 K shown by the black arrow. (b) x = 0.115. The linear increase of $I_{fast}$ starts at $T_{charge} \sim 80$ K. (c) x = 0.10. There is a precursor behavior starting at $\sim$ 100 K, where $I_{fast}$ slowly emerges, which we presume is associated to charge localization effects. However, the linear increase of $I_{fast}$ begins at $\sim$ 65 K, which we consider as $T_{charge}$.

The temperature dependence of the average, fast and slow components of $1/T_1$ for x = 0.10 in $B_{ext}$ || c are shown in Fig. 3.7(c). Our stretched fit results are consistent with earlier reports [20, 43]. 10% has a slower enhancement of $1/T_1$ at low temperatures and does not reach a peak, meaning that spins are still slowing down even at the base temperatures. $1/T_1^{fast}$ and $1/T_1^{slow}$ behave very similarly to 13%; $1/T_1^{fast}$ follows the average $1/T_1$ by strongly increasing at low temperature, while $1/T_1^{slow}$ decreases down to $\sim$ 15 K. Thus, $1/T_1^{fast}$ is characteristic of a stripe ordered state, while $1/T_1^{slow}$ follows d-wave superconducting behaviour.

As seen in Fig. 3.8(c), $I_{slow}$ deviates slightly from one near $\sim$ 100 K. We attribute this precursor behavior to charge localization, as discussed in detail by Hunt et al. in the context of the charge order phase diagram of the Nd and Eu co-doped $La_{2-x}Sr_xCuO_4$ in their Fig. 18 [18]. The localization of holes creates local moments where mobile holes would be located that gradually enhance $1/T_1$ [19]. Transport measurements of $La_{2-x}Sr_xCuO_4$ have observed charge localization that sets in at higher temperature than $T_{charge}$ below the optimal stripe order doping of x $\sim$ 1/8 [14]. Thus, we deduce that localization effects will induce fast relaxation even before charge order sets in. $I_{slow}$ begins to decrease roughly linearly starting from $\sim$ 65 K. We therefore conclude that $T_{charge} = 65^{+12}_{-10}$ K.

We summarize our findings of $T_{charge}$ for x = 0.13, 0.115 and 0.10 of $La_{2-x}Sr_xCuO_4$ in a phase diagram in Fig. 3.9 [32]. The colour gradient in the charge order dome represents increasing volume fraction of $1/T_1^{fast}$ by increments of 25% from light to dark regions. Interestingly, the spin ordering temperature at the neutron scattering timescale coincides with the temperature at which $\sim$ 75% of the sample is quickly relaxing. Notice that He et al.'s x-ray scattering and our NMR data are in

excellent agreement for the same 11.5% crystal [23]. However, our data differs from Croft et al.'s x-ray scattering data, which shows a half-dome peaked at $\sim$ 13%. This discrepancy might be from slight deviation in the doping concentration, since e.g. the oxygen concentration also affects the phase diagram [33].

## 3.6 Conclusions

In this paper, we have presented comprehensive $^{139}$La NMR measurements of $La_{2-x}Sr_xCuO_4$ for x = 0.13 and x = 0.10 and compared our results with our previous work on $La_{1.885}Sr_{0.115}CuO_4$. We have estimated the onset temperature of charge and spin ordering; the linear increase of the volume fraction of $1/T_1^{fast}$ indicates the onset of charge order, while the dramatic enhancement of $\Delta$f at low temperatures indicates the spin order at the neutron scattering timescale, both summarized in Table. 3.1.

We were able to map the charge order dome and elucidate the effect of charge order on spin fluctuations of $La_{2-x}Sr_xCuO_4$. By splitting the relaxation rate into a fast and slow component, in accordance with the presence of two different types of $^{63}$Cu NMR signals in the charge ordered state [24], we were able to deduce the volume fraction under the influence of stripe order below $T_{charge}$. The phase diagram in Fig. 3.9 suggests that, in agreement with the recent transport measurements [46, 47], $T_{charge}$ decreases above and below $x \sim 1/8$.

We showed that below $T_{charge}$, two different phases exist in the sample volume: the superconducting state with slow relaxation, and the charge ordered state with

faster relaxation. Although we cannot confirm whether both states are phase separated or coexistent, our measurements confirm the close competition between d-wave superconductivity and stripe order found in some theoretical studies of the t-J model [48–50].

Our new approach based on the two component fit of $^{139}$La $1/T_1$ can be applied to other $La_2CuO_4$-based cuprates such as $La_2CuO_{4+y}$ [51]. Moreover, our preliminary $^{139}$La single crystal NMR results in $La_{1.875}Ba_{0.125}CuO_4$ indicate that $I_{fast}$ increases very quickly below $T_{charge} \sim 55$ K [52]. This may be an indication that charge ordered domains can grow much faster in the LTT phase. We will discuss the complete details elsewhere.

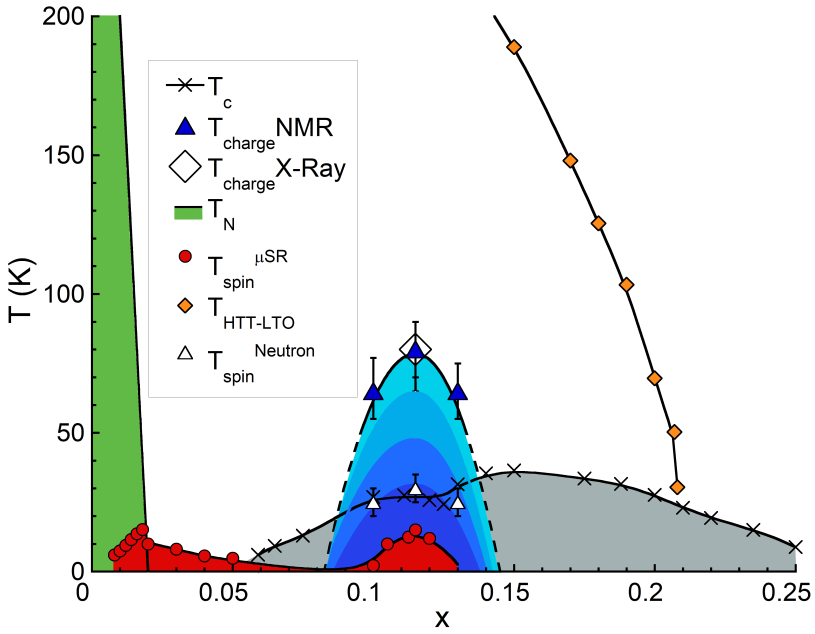


FIGURE 3.9: Phase diagram of $La_{2-x}Sr_xCuO_4$ showing the charge order temperature, $T_{charge}$ (▲) obtained for x = 0.10 and x = 0.13 (this work) and x = 0.115 [32], $T_{charge}$ (◇) reported by x-ray data [23], the spin order temperature (●) reported by $\mu$SR [53] and NQR [54] and the superconducting critical temperature $T_c$ (×) [55]. The structural phase transition (◆) temperature was reproduced from Takagi et al. [56]. The spin order at the neutron scattering timescale (△) found in this paper and in [32] is also shown. The antiferromagnetic boundary was reproduced from [54]. Darker blue regions of the charge order dome represent increasing fast volume fraction in increments of 25%.

## 3.7 Acknowledgement

The work at McMaster was financially supported by NSERC and CIFAR. The work at Tohoku was supported by Grant-in-Aid for Scientific Research (A) (16H02125), Japan.

## 3.8 Appendix A: $f_0$ and $\Delta f$

Fig. 3.10 shows the peak of the lineshape, $f_0$ versus temperature for the three doping levels. The orange arrow marks the structural phase transition, where $f_0$ begins to decrease. x = 0.10 has $T_{HTT-LTO}$ greater than 295 K, so it is not shown. Our $T_{HTT-LTO}$ measurements are consistent with recent NMR measurements by Baek et al. [43]. Notice that the peak frequency decreases through the structural phase transition from the high temperature tetragonal (HTT) to the low temperature orthorhombic (LTO), down to $\sim$ 100 K, more evidently for $B_{ext}$ || c than for $B_{ext}$ || ab. This is because the main principal axis of the EFG tensor at the $^{139}$La sites is parallel to the c-axis in the HTT phase and hence, there is no second order quadrupole shift. However, for $B_{ext}$ || ab, $\Delta\nu_Q^{(2)}$ is large and positive. The structural phase transition tilts the $CuO_6$ octahedra, causing a decrease in $\Delta\nu_Q^{(2)}$ that lowers the resonance frequency.

We show the temperature dependence of $\Delta f$ in Fig. 3.11. At high temperatures for $B_{ext}$ || c, the lack of second order quadrupole shift makes the lineshapes very narrow. Due to a distribution of tilting angles and $\nu_Q$, the linewidth increases

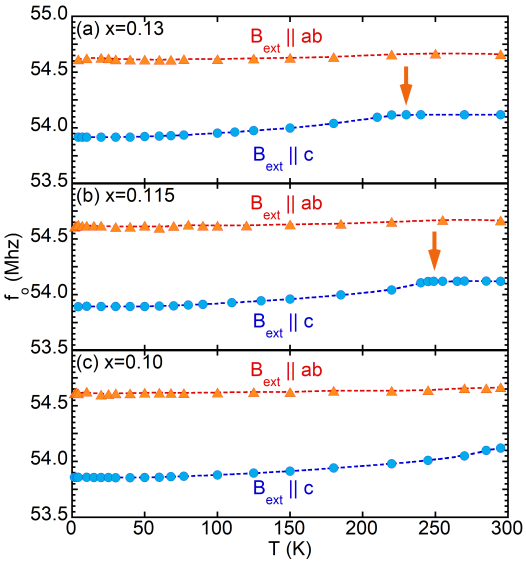


FIGURE 3.10: (a) x = 0.13, (b) x = 0.115, and (c) x = 0.10 $^{139}$La NMR resonance frequency, $f_0$, in $B_{ext}$ = 9 T versus temperature. The orange arrow marks the HTT to LTO structural phase transition. For x = 0.10, $T_{HTT-LTO}$ is above 300 K, so it has not been measured.

through the structural phase transition. We find that the linewidth slightly increases when charge order sets in. However, we verified for 11.5% that the line broadening was paramagnetic in origin, rather than quadrupolar by measuring $\Delta f$ in 4.5 T [32]. For x = 0.13, the slight broadening corresponding to the charge ordering temperature is located at $T_{charge} \sim 65$ K. In the case of $La_{1.885}Sr_{0.115}CuO_4$, we demonstrated that additional line broadening sets in at $\sim$ 5 K above the onset of spin order with the measurement time scale of elastic neutron scattering $T_{spin}^{Neutron}$ due to the emergence of a nearly static hyperfine magnetic field within the ab-plane. Therefore, we identify the onset of spin order as $T_{spin}^{Neutron} \sim 25$ K for x = 0.13 according to the dramatic enhancement of $\Delta f$. Since the crystal axes were rotated from the sample surface for the x = 0.13 crystal, achieving perfect alignment with $B_{ext}$ proved to be difficult. For that reason (and the added $Sr^{2+}$

disorder), the linewidth measured for x = 0.13 with $B_{ext}$ || ab is somewhat larger than for x = 0.10 and 0.115 due to potential misalignment by $\sim 2°$. We note however that the main evidence for $T_{charge}$ used in this paper is for $B_{ext}$ || c.

The slight enhancement of the linewidth for x = 0.10 occurs at $T_{charge} \sim 65$ K, in agreement with the double component analysis. The spin order at the neutron scattering timescale according to the analogous dramatic line broadening for x = 0.10 is $T_{spin}^{Neutron} \sim 25$ K, consistent with measurements done by Chang et al. [57]. Our $\Delta$f results are very similar to the pioneering powder $^{139}$La NMR measurements of $La_{2-x}Sr_xCuO_4$ by Goto et al. [58, 59]; their linewidth was measured only below 60 K, however, since charge order had not been discovered when they initiated their work.

## 3.9 Appendix B: Stretched Fit Relaxation Curves

Figs. 3.12(a) and (b) show relaxation curves at select temperatures for x = 0.13 and x = 0.10 fit with the stretched fit from Eq. 3.1. We normalized the data so that A = B = 1 for a clearer comparison of the data at different temperatures. We refer the reader to [32] for x = 0.115 relaxation curves. Notice that both the double component fit in Fig. 3.6 and the stretched fit in Fig. 3.12 are good fits for the data, which explains why some earlier publications overlooked the emergence of two separate components below $T_{charge}$.

Figs. 3.12(c), (d) and (e) show the temperature dependence of $\beta$ for all doping concentrations measured. $\beta$ deviates from one at the structural phase transition,

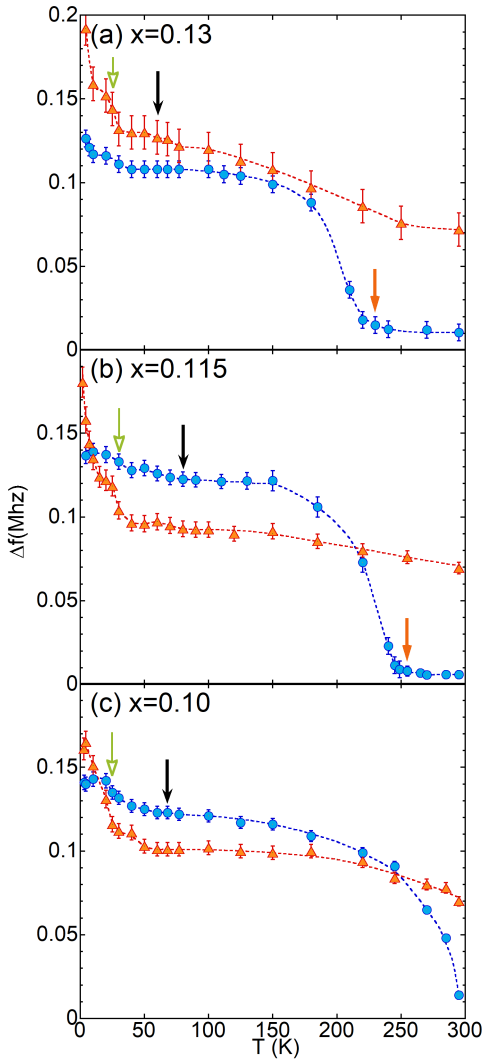


FIGURE 3.11: Half width at half maximum (HWHM), $\Delta f$, of the lineshapes at different temperatures. Dashed lines are guides for the eye. (a) x = 0.13. $T_{charge} \sim 65$ K, where a slight line broadening sets in (black arrow). $T_{spin}^{Neutron}$ is linked to the dramatic line broadening at $\sim$ 25 K (green arrow). $T_{HTT-LTO} \sim 230$ K is marked by the enhanced broadening for $B_{ext} \parallel$ c (orange arrow). (b) x = 0.115 [32]. $T_{charge} \sim 80$ K, while $T_{spin}^{Neutron} \sim 30$ K and $T_{HTT-LTO} \sim 250$ K. (c) x = 0.10. $T_{charge} \sim 65$ K and $T_{spin}^{Neutron} \sim 25$ K. The line broadening from the structural phase transition begins at >295 K.

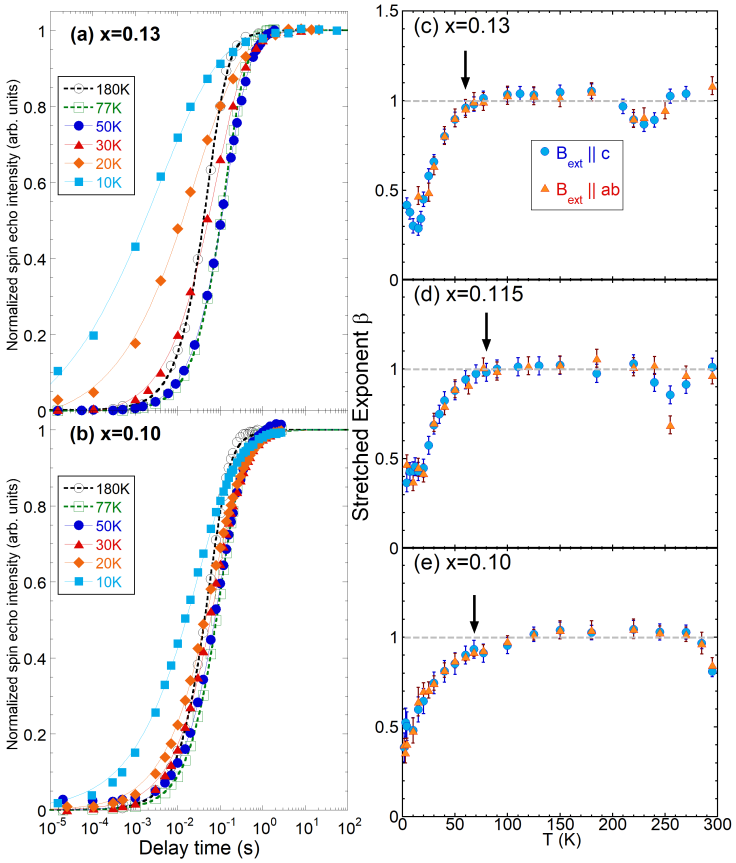


FIGURE 3.12: Spin-lattice relaxation curves fit to a stretched fit for (a) x = 0.13 and (b) x = 0.10. See [32] for 11.5% relaxation curves. Temperature dependence of the phenomenological parameter $\beta$ for both $B_{ext}$ || c (blue) and $B_{ext}$ || ab (orange) for (c) x = 0.13, (d) x = 0.115 and (e) x = 0.10.

as expected from quadrupolar effects. $\beta$ also deviates from one at $T_{charge}$, marked by the black arrow, due to a distribution of $1/T_1$. For x = 0.10, $\beta$ deviates from one at $\sim$ 100 K due to charge localization.

# Chapter 4

# Conclusion

This thesis presented our recent $^{139}$La NMR work on $La_{2-x}Sr_xCuO_4$ with doping concentrations of x=0.13, 0.115 and 0.10. We revisited Hunt et al.'s pioneering $^{63}$Cu NQR work by indirectly probing the charge order temperature of $La_{2-x}Sr_xCuO_4$ based on $^{139}$La NMR, and showed that $T_{charge}$ decreases below x $\sim$ 1/8. By analysing the lineshapes, spin-lattice relaxation rate and volume fractions, we were able to elucidate the charge order dome of the $La_{2-x}Sr_xCuO_4$ phase diagram. We found that the dome is peaked at x $\sim$ 0.115 and showed that our $^{139}$La NMR work is consistent with recent x-ray scattering and $^{63}$Cu NMR experiments. Relaxation rate measurements also gave us the structural phase transition and spin ordering temperatures.

The method of double component fit used in this thesis can also be used on other $La_2CuO_4$-based superconductors. Due to the irrefutable evidence of charge order in $La_{2-x-y}(Nd,Eu)_ySr_xCuO_4$, obtaining $^{139}$La NMR double component data would be interesting to see how the fast relaxation rate behaves compared to the slow one in co-doped materials. We have initiated measurements in $La_{2-x}Ba_xCuO_4$ and

using the double component analysis, $I_{fast}$ emerges very quickly below the charge order temperature at $T_{charge} \sim 55$ K, as previously determined by Bragg scattering experiments. The quick emergence of $I_{fast}$ is most likely due to the obvious LTT transition observed in $La_{2-x}Ba_xCuO_4$ that pins the charge order.

# Chapter 5

# Appendix: Copyright Permissions

Below are the copyright permissions obtained for figures 1.1, 1.3, 1.6, 1.7, 1.8, 2.7, 2.9 and 3.1 to 3.4 in the order they appear in the thesis. Copyright permissions for unpublished work will be obtained once published.

SPRINGER NATURE

| | |
|---|---|
| **Title:** | From quantum matter to high-temperature superconductivity in copper oxides |
| **Author:** | B. Keimer, S. A. Kivelson, M. R. Norman, S. Uchida, J. Zaanen |
| **Publication:** | Nature |
| **Publisher:** | Springer Nature |
| **Date:** | Feb 11, 2015 |





## Order Completed

Thank you for your order.

This Agreement between McMaster University -- Alexandre Arsenault ("You") and Springer Nature ("Springer Nature") consists of your license details and the terms and conditions provided by Springer Nature and Copyright Clearance Center.

Your confirmation email will contain your order number for future reference.

printable details

| | |
|---|---|
| License Number | 4414920377960 |
| License date | Aug 23, 2018 |
| Licensed Content Publisher | Springer Nature |
| Licensed Content Publication | Nature |
| Licensed Content Title | From quantum matter to high-temperature superconductivity in copper oxides |
| Licensed Content Author | B. Keimer, S. A. Kivelson, M. R. Norman, S. Uchida, J. Zaanen |
| Licensed Content Date | Feb 11, 2015 |
| Licensed Content Volume | 518 |
| Licensed Content Issue | 7538 |
| Type of Use | Thesis/Dissertation |
| Requestor type | academic/university or research institute |
| Format | electronic |
| Portion | figures/tables/illustrations |
| Number of figures/tables/illustrations | 1 |
| High-res required | no |
| Will you be translating? | no |
| Circulation/distribution | <501 |
| Author of this Springer Nature content | no |
| Title | Master's Student |
| Instructor name | Takashi Imai |
| Institution name | McMaster University |
| Expected presentation date | Aug 2018 |
| Portions | Figure 3 |
| Requestor Location | McMaster University<br>210 Winston Place |

| | |
|---|---|
| | Hamilton, ON L8S 2S9<br>Canada<br>Attn: Alexandre Arsenault |
| Billing Type | Invoice |
| Billing address | McMaster University<br>210 Winston Place<br><br>Hamilton, ON L8S 2S9<br>Canada<br>Attn: Alexandre Arsenault |
| Total | 0.00 CAD |

ORDER MORE CLOSE WINDOW

## Order Completed

Thank you for your order.

This Agreement between McMaster University -- Alexandre Arsenault ("You") and Springer Nature ("Springer Nature") consists of your license details and the terms and conditions provided by Springer Nature and Copyright Clearance Center.

Your confirmation email will contain your order number for future reference.

printable details

| | |
|---|---|
| License Number | 4414920926235 |
| License date | Aug 23, 2018 |
| Licensed Content Publisher | Springer Nature |
| Licensed Content Publication | Nature |
| Licensed Content Title | Evidence for stripe correlations of spins and holes in copper oxide superconductors |
| Licensed Content Author | J. M. Tranquada, B. J. Sternlieb, J. D. Axe, Y. Nakamura, S. Uchida |
| Licensed Content Date | Jun 15, 1995 |
| Licensed Content Volume | 375 |
| Licensed Content Issue | 6532 |
| Type of Use | Thesis/Dissertation |
| Requestor type | academic/university or research institute |
| Format | electronic |
| Portion | figures/tables/illustrations |
| Number of figures/tables/illustrations | 1 |
| Will you be translating? | no |
| Circulation/distribution | <501 |
| Author of this Springer Nature content | no |
| Title | Master's Student |
| Instructor name | Takashi Imai |
| Institution name | McMaster University |
| Expected presentation date | Aug 2018 |
| Portions | Figure 1 |
| Requestor Location | McMaster University<br>210 Winston Place |

| | |
|---|---|
| | Hamilton, ON L8S 2S9<br>Canada<br>Attn: Alexandre Arsenault |
| Billing Type | Invoice |
| Billing address | McMaster University<br>210 Winston Place<br><br>Hamilton, ON L8S 2S9<br>Canada<br>Attn: Alexandre Arsenault |
| Total | 0.00 USD |

ORDER MORE CLOSE WINDOW

# American Physical Society
# Reuse and Permissions License

23-Aug-2018

This license agreement between the American Physical Society ("APS") and Alexandre Arsenault ("You") consists of your license details and the terms and conditions provided by the American Physical Society and SciPris.

## Licensed Content Information

| | |
|---|---|
| **License Number:** | **RNP/18/AUG/007107** |
| **License date:** | 23-Aug-2018 |
| **DOI:** | 10.1103/PhysRevB.70.060503 |
| **Title:** | Electron localization in ${\mathrm{La}}_{2-x}{\mathrm{Sr}}_{x}\mathrm{Cu}{\mathrm{O}}_{4}$ and the role of stripes |
| **Author:** | Seiki Komiya and Yoichi Ando |
| **Publication:** | Physical Review B |
| **Publisher:** | American Physical Society |
| **Cost:** | USD $ 0.00 |

## Request Details

**Does your reuse require significant modifications**: No

| | |
|---|---|
| **Specify intended distribution locations:** | Worldwide |
| **Reuse Category:** | Reuse in a thesis/dissertation |
| **Requestor Type:** | Student |
| **Items for Reuse:** | Figures/Tables |
| **Number of Figure/Tables:** | 1 |
| **Figure/Tables Details:** | Figure 1 |
| **Format for Reuse:** | Electronic |

## Information about New Publication:

| | |
|---|---|
| **University/Publisher:** | McMaster Univerity |
| **Title of dissertation/thesis:** | La NMR Charge Order Study of LSCO |
| **Author(s):** | Alexandre Arsenault |
| **Expected completion date:** | Aug. 2018 |

## License Requestor Information

| | |
|---|---|
| **Name:** | Alexandre Arsenault |
| **Affiliation:** | Individual |
| **Email Id:** | alex.ars@hotmail.ca |
| **Country:** | Canada |

# American Physical Society
# Reuse and Permissions License

23-Aug-2018

This license agreement between the American Physical Society ("APS") and Alexandre Arsenault ("You") consists of your license details and the terms and conditions provided by the American Physical Society and SciPris.

## Licensed Content Information

| | |
|---|---|
| **License Number:** | **RNP/18/AUG/007108** |
| **License date:** | 23-Aug-2018 |
| **DOI:** | 10.1103/PhysRevB.64.134525 |
| **Title:** | Glassy slowing of stripe modulation in ${(\mathrm{L}\mathrm{a},\mathrm{E}\mathrm{u},\mathrm{N}\mathrm{d})}_{2-x}({\mathrm{S}\mathrm{r},\mathrm{B}\mathrm{a})}_{x}{\mathrm{CuO}}_{4}:\mathrm{A}{}^{63}\mathrm{Cu}$ and ${}^{139}\mathrm{La}$ NQR study down to 350 mK |
| **Author:** | A. W. Hunt et al. |
| **Publication:** | Physical Review B |
| **Publisher:** | American Physical Society |
| **Cost:** | USD $ 0.00 |

## Request Details

**Does your reuse require significant modifications**: No

| | |
|---|---|
| **Specify intended distribution locations:** | Worldwide |
| **Reuse Category:** | Reuse in a thesis/dissertation |
| **Requestor Type:** | Student |
| **Items for Reuse:** | Figures/Tables |
| **Number of Figure/Tables:** | 1 |
| **Figure/Tables Details:** | Figure 18 |
| **Format for Reuse:** | Electronic |

## Information about New Publication:

| | |
|---|---|
| **University/Publisher:** | McMaster University |
| **Title of dissertation/thesis:** | La NMR Charge Order Study of LSCO |
| **Author(s):** | Alexandre Arsenault |
| **Expected completion date:** | Aug. 2018 |

## License Requestor Information

| | |
|---|---|
| **Name:** | Alexandre Arsenault |
| **Affiliation:** | Individual |
| **Email Id:** | alex.ars@hotmail.ca |
| **Country:** | Canada |

# American Physical Society
# Reuse and Permissions License

23-Aug-2018

This license agreement between the American Physical Society ("APS") and Alexandre Arsenault ("You") consists of your license details and the terms and conditions provided by the American Physical Society and SciPris.

## Licensed Content Information

| | |
|---|---|
| **License Number:** | **RNP/18/AUG/007110** |
| **License date:** | 23-Aug-2018 |
| **DOI:** | 10.1103/PhysRevB.96.224508 |
| **Title:** | Revisiting $^{63}\mathrm{Cu}$ NMR evidence for charge order in superconducting ${\mathrm{La}}_{1.885}{\mathrm{Sr}}_{0.115}{\mathrm{CuO}}_{4}$ |
| **Author:** | T. Imai et al. |
| **Publication:** | Physical Review B |
| **Publisher:** | American Physical Society |
| **Cost:** | USD $ 0.00 |

## Request Details

**Does your reuse require significant modifications**: No

| | |
|---|---|
| **Specify intended distribution locations:** | Worldwide |
| **Reuse Category:** | Reuse in a thesis/dissertation |
| **Requestor Type:** | Student |
| **Items for Reuse:** | Figures/Tables |
| **Number of Figure/Tables:** | 1 |
| **Figure/Tables Details:** | Figure 7(b) |
| **Format for Reuse:** | Electronic |

## Information about New Publication:

| | |
|---|---|
| **University/Publisher:** | McMaster University |
| **Title of dissertation/thesis:** | La NMR Charge Order Study of LSCO |
| **Author(s):** | Alexandre Arsenault |
| **Expected completion date:** | Aug. 2018 |

## License Requestor Information

| | |
|---|---|
| **Name:** | Alexandre Arsenault |
| **Affiliation:** | Individual |
| **Email Id:** | alex.ars@hotmail.ca |
| **Country:** | Canada |

# American Physical Society
# Reuse and Permissions License

23-Aug-2018

This license agreement between the American Physical Society ("APS") and Alexandre Arsenault ("You") consists of your license details and the terms and conditions provided by the American Physical Society and SciPris.

## Licensed Content Information

| | |
|---|---|
| **License Number:** | **RNP/18/AUG/007111** |
| **License date:** | 23-Aug-2018 |
| **DOI:** | 10.1103/PhysRevB.87.174505 |
| **Title:** | Structural transitions in a doped lanthanum cuprate |
| **Author:** | S.-H. Baek et al. |
| **Publication:** | Physical Review B |
| **Publisher:** | American Physical Society |
| **Cost:** | USD $ 0.00 |

## Request Details

**Does your reuse require significant modifications**: No

| | |
|---|---|
| **Specify intended distribution locations:** | Worldwide |
| **Reuse Category:** | Reuse in a thesis/dissertation |
| **Requestor Type:** | Student |
| **Items for Reuse:** | Figures/Tables |
| **Number of Figure/Tables:** | 1 |
| **Figure/Tables Details:** | Figure 4 |
| **Format for Reuse:** | Electronic |

## Information about New Publication:

| | |
|---|---|
| **University/Publisher:** | McMaster University |
| **Title of dissertation/thesis:** | La NMR Charge Order Study of LSCO |
| **Author(s):** | Alexandre Arsenault |
| **Expected completion date:** | Aug. 2018 |

## License Requestor Information

| | |
|---|---|
| **Name:** | Alexandre Arsenault |
| **Affiliation:** | Individual |
| **Email Id:** | alex.ars@hotmail.ca |
| **Country:** | Canada |

# American Physical Society
# Reuse and Permissions License

23-Aug-2018

This license agreement between the American Physical Society ("APS") and Alexandre Arsenault ("You") consists of your license details and the terms and conditions provided by the American Physical Society and SciPris.

## Licensed Content Information

| | |
|---|---|
| **License Number:** | **RNP/18/AUG/007112** |
| **License date:** | 23-Aug-2018 |
| **DOI:** | 10.1103/PhysRevLett.98.047002 |
| **Title:** | Spin Triplet Superconducting State due to Broken Inversion Symmetry in ${\mathrm{Li}}_{2}{\mathrm{Pt}}_{3}\mathrm{B}$ |
| **Author:** | M. Nishiyama, Y. Inada, and Guo-qing Zheng |
| **Publication:** | Physical Review Letters |
| **Publisher:** | American Physical Society |
| **Cost:** | USD $ 0.00 |

## Request Details

**Does your reuse require significant modifications**: No

| | |
|---|---|
| **Specify intended distribution locations:** | Worldwide |
| **Reuse Category:** | Reuse in a thesis/dissertation |
| **Requestor Type:** | Student |
| **Items for Reuse:** | Figures/Tables |
| **Number of Figure/Tables:** | 1 |
| **Figure/Tables Details:** | Figure 3 |
| **Format for Reuse:** | Electronic |

## Information about New Publication:

| | |
|---|---|
| **University/Publisher:** | McMaster University |
| **Title of dissertation/thesis:** | La NMR Charge Order Study of LSCO |
| **Author(s):** | Alexandre Arsenault |
| **Expected completion date:** | Aug. 2018 |

## License Requestor Information

| | |
|---|---|
| **Name:** | Alexandre Arsenault |
| **Affiliation:** | Individual |
| **Email Id:** | alex.ars@hotmail.ca |
| **Country:** | Canada |

# American Physical Society
# Reuse and Permissions License

23-Aug-2018

This license agreement between the American Physical Society ("APS") and Alexandre Arsenault ("You") consists of your license details and the terms and conditions provided by the American Physical Society and SciPris.

## Licensed Content Information

| | |
|---|---|
| **License Number:** | **RNP/18/AUG/007113** |
| **License date:** | 23-Aug-2018 |
| **DOI:** | 10.1103/PhysRevB.97.064511 |
| **Title:** | $^{139}\mathrm{La}$ |
| **Author:** | A. Arsenault et al. |
| **Publication:** | Physical Review B |
| **Publisher:** | American Physical Society |
| **Cost:** | USD $ 0.00 |

## Request Details

**Does your reuse require significant modifications**: No

| | |
|---|---|
| **Specify intended distribution locations:** | Worldwide |
| **Reuse Category:** | Reuse in a thesis/dissertation |
| **Requestor Type:** | Author of requested content |
| **Items for Reuse:** | Figures/Tables |
| **Number of Figure/Tables:** | 4 |
| **Figure/Tables Details:** | Figure 1, 2, 3, 5 |
| **Format for Reuse:** | Electronic |

## Information about New Publication:

| | |
|---|---|
| **University/Publisher:** | McMaster University |
| **Title of dissertation/thesis:** | La NMR Charge Order Study of LSCO |
| **Author(s):** | Alexandre Arsenault |
| **Expected completion date:** | Aug. 2018 |

## License Requestor Information

| | |
|---|---|
| **Name:** | Alexandre Arsenault |
| **Affiliation:** | Individual |
| **Email Id:** | alex.ars@hotmail.ca |
| **Country:** | Canada |

# Bibliography


[1] N. Mott, Proc. Phys. Soc. A **62**, 416 (1949).

[2] J. G. Bednorz and K. A. Muller, Z. Phys. B -Condensed Matter **64**, 189 (1986).

[3] C. W. Chu, L. Z. Deng, and B. Lv, arXiv **1502**, 04686 (2015).

[4] A. Shah, Translational Research in Coronary Artery Disease , 153 (2016).

[5] T. Ito, H. Takagi, S. Ishibashi, T. Ido, and S. Uchida, Nature **350**, 596 (1991).

[6] B. Keimer, S. A. Kivelson, M. R. Norman, S. Uchida, and J. Zaanen, Nature **518**, 179 (2015).

[7] M. Greven, http://www.mrsec.umn.edu/research/seeds/2011/greven2011.html , 1 (2018).

[8] G. Luke, L. Le, B. Sternlieb, W. Wu, Y. Uemura, J. Brewer, T. Riseman, S. Ishibashi, and S. Uchida, Physica C: Superconductivity **185-189**, 1175 (1991).

[9] J. M. Tranquada, J. D. Axe, N. Ichikawa, Y. Nakamura, S. Uchida, and B. Nachumi, Phys. Rev. B **54**, 7489 (1996).

[10] N. Ichikawa, S. Uchida, J. M. Tranquada, T. Niemöller, P. M. Gehring, S.-H. Lee, and J. R. Schneider, Phys. Rev. Lett. **21**, 1738 (2000).

[11] B. Nachumi, Y. Fudamoto, A. Keren, K. M. Kojima, M. Larkin, G. M. Luke, J. Merrin, O. Tchernyshyov, Y. J. Uemura, N. Ichikawa, M. Goto, H. Takagi, S. Uchida, M. K. Crawford, E. M. Mccarron, D. E. Maclaughlin, and R. H. Heffner, Phys. Rev. B **58**, 13 (1998).

[12] J. Tranquada, B. Sternlieb, J. Axe, Y. Nakamura, and S. Uchida, Nature **375** (1995).

[13] A. R. Moodenbaugh, L. Wu, Y. Zhu, L. H. Lewis, and D. E. Cox, Phys. Rev. B **58**, 14 (1998).

[14] S. Komiya and Y. Ando, Phys. Rev. B **70**, 060503 (2004).

[15] M. N. Khlopkin, G. K. Panova, N. A. Chernoplekov, A. A. Shikov, and A. V. Suetin, Journal of Theoretical and Experimental Physics **112**, 1386 (1996).

[16] J. Bardeen, L. N. Cooper, and J. R. Schrieffer, Phys. Rev. **108**, 5 (1957).

[17] C. A. Reynolds, B. Serin, W. H. Wright, and L. B. Nesbitt, Phys. Rev. **78**, 487 (1950).

[18] A. W. Hunt, P. M. Singer, A. F. Cederströ, and T. Imai, Phys. Rev. B **64**, 134525 (2001).

[19] A. W. Hunt, P. M. Singer, K. R. Thurber, and T. Imai, Physical Review Letters **82**, 4300 (1999).

[20] M.-H. Julien, A. Campana, A. Rigamonti, P. Carretta, F. Borsa, P. Kuhns, A. P. Reyes, W. G. Moulton, M. Horvati, C. Berthier, A. Vietkin, and A. Revcolevschi, Phys. Rev. B **63**, 144508 (2001).

[21] N. J. Curro, P. C. Hammel, B. J. Suh, M. Hücker, B. Büchner, U. Ammerahl, and A. Revcolevschi, Phys. Rev. Lett. **85**, 3 (2000).

[22] T. P. Croft, C. Lester, M. S. Senn, A. Bombardi, and S. M. Hayden, Phys. Rev. B **89**, 224513 (2014).

[23] W. He, Y. S. Lee, and M. Fujita, (To be published) .

[24] T. Imai, S. K. Takahashi, A. Arsenault, A. W. Acton, D. Lee, W. He, Y. S. Lee, and M. Fujita, Phys. Rev. B **96**, 224508 (2017).

[25] C. P. Slichter, *Principles of Magnetic Resonance*, 2nd ed. (Springer, 1978).

[26] A. Abragam, *The Principles of Nuclear Magnetism* (Oxford University Press, 1961).

[27] R. M. White, *Quantum Theory of Magnetism*, 3rd ed. (Springer, 2007).

[28] V. Jaccarino, *Theory of magnetism in transition metals ed. W. Marshall* (Academic Press, 1967).

[29] S.-H. Baek, P. C. Hammel, M. Hücker, B. Büchner, U. Ammerahl, A. Revcolevschi, and B. J. Suh, Phys. Rev. B **87**, 174505 (2013).

[30] L. C. Hebel and C. P. Slichter, Phys. Rev. **113**, 6 (1959).

[31] B. M. Nishiyama, Y. Inada, and G. Zheng, Phys. Rev. Lett. **98**, 047002 (2007).

[32] A. Arsenault, S. K. Takahashi, T. Imai, W. He, Y. S. Lee, and M. Fujita, Phys. Rev. B **97**, 064511 (2018).

[33] K. Yoshimura, T. Uemura, M. Kato, T. Shibata, K. Kosuge, T. Imai, and H. Yasuoka, Springer Proc. in Phys. **60**, 405 (1992).

[34] E. H. da Silva Neto, P. Aynajian, A. Frano, R. Comin, E. Schierle, E. Weschke, A. Gyenis, J. Wen, J. Schneeloch, Z. Xu, S. Ono, G. Gu, M. Le Tacon, and A. Yazdani, Science (New York, N.Y.) **343**, 393 (2014).

[35] R. Comin, A. Frano, M. M. Yee, Y. Yoshida, H. Eisaki, E. Schierle, E. Weschke, R. Sutarto, F. He, A. Soumyanarayanan, Y. He, M. Le Tacon, I. S. Elfimov, J. E. Hoffman, G. A. Sawatzky, B. Keimer, and A. Damascelli, Science (New York, N.Y.) **343**, 390 (2014).

[36] W. Tabis, Y. Li, M. L. Tacon, L. Braicovich, A. Kreyssig, M. Minola, G. Dellea, E. Weschke, M. J. Veit, M. Ramazanoglu, A. I. Goldman, T. Schmitt, G. Ghiringhelli, N. Barišić, M. K. Chan, C. J. Dorow, G. Yu, X. Zhao, B. Keimer, and M. Greven, Nature Communications **5**, 5875 (2014).

[37] G. Ghiringhelli, M. Le Tacon, M. Minola, S. Blanco-Canosa, C. Mazzoli, N. B. Brookes, G. M. De Luca, A. Frano, D. G. Hawthorn, F. He, T. Loew, M. Moretti Sala, D. C. Peets, M. Salluzzo, E. Schierle, R. Sutarto, G. A. Sawatzky, E. Weschke, B. Keimer, and L. Braicovich, Science **295**, 466 (2002).

[38] S. Kawasaki, Z. Li, M. Kitahashi, C. T. Lin, P. L. Kuhns, A. P. Reyes, and G.-q. Zheng, Nature Communications **8**, 1267 (2017).

[39] T. Wu, H. Mayaffre, S. Krämer, M. Horvatić, C. Berthier, W. N. Hardy, R. Liang, D. A. Bonn, and M.-H. Julien, Nature **477**, 191 (2011).

[40] V. Thampy, M. P. M. Dean, N. B. Christensen, L. Steinke, Z. Islam, M. Oda, M. Ido, N. Momono, S. B. Wilkins, and J. P. Hill, Phys. Rev. B **90**, 100510 (2014).

[41] T. Imai and K. Hirota, Unpublished $^{63}$Cu, $^{139}$La, and $^{17}$O NMR work on a $La_{1.885}Sr_{0.115}CuO_4$ single crystal presented first at the Aspen Winter Conference on Quantum Criticality (January 1999).

[42] V. F. Mitrović, M.-H. Julien, C. De Vaulx, M. Horvatić, C. Berthier, T. Suzuki, and K. Yamada, Phys. Rev. B **78**, 014504 (2008).

[43] S.-H. Baek, A. Erb, and B. Büchner, Phys. Rev. B **96**, 094519 (2017).

[44] E. R. Andrew and D. P. Tunstall, Proc. Phys. Soc **78**, 1 (1961).

[45] A. Narath, Phys. Rev. **162**, 320 (1967).

[46] Y. Ando, S. Komiya, K. Segawa, S. Ono, and Y. Kurita, Phys. Rev. Lett. **93**, 267001 (2004).

[47] S. Badoux, S. A. A Afshar, B. Michon, A. Ouellet, S. Fortier, D. LeBoeuf, T. P. Croft, C. Lester, S. M. Hayden, H. Takagi, K. Yamada, D. Graf, N. Doiron-Leyraud, and L. Taillefer, Phys. Rev. X **6**, 021004 (2016).

[48] S. A. Kivelson, G. Aeppli, and V. J. Emery, Proc. Nat. Acad. Sci. **98**, 11903 (2001).

[49] A. Himeda, T. Kato, and M. Ogata, Phys. Rev. Lett. **88**, 117001 (2002).

[50] P. Corboz, T. M. Rice, and M. Troyer, Phys. Rev. Lett. **113**, 046402 (2014).

[51] T. Imai and Y. S. Lee, Phys. Rev. B **97**, 104506 (2018).

[52] M. Fujita, H. Goka, K. Yamada, J. M. Tranquada, and L. P. Regnault, Phys. Rev. B **70**, 104517 (2004).

[53] K.-I. Kumagai, K. Kawano, I. Watanabe, K. Nishiyama, and K. Nagamine, Hyperfine Interactions **86**, 473 (1994).

[54] F. C. Chou, F. Borsa, J. H. Cho, D. C. Johnston, A. Lascialfari, D. R. Torgeson, and J. Ziolo, Phys. Rev. Lett. **71**, 14 (1993).

[55] H. Takagi, T. Ido, S. Ishibashi, M. Uota, S. Uchida, and Y. Tokura, Phys. Rev. B **40**, 2254 (1989).

[56] H. Takagi, R. J. Cava, M. Marezio, B. Batlogg, J. J. Krajewski, W. F. Peck, P. Bordet, and D. E. Cox, Phys. Rev. Lett. **68**, 25 (1992).

[57] J. Chang, C. Niedermayer, R. Gilardi, N. B. Christensen, H. M. Rønnow, D. F. Mcmorrow, M. Ay, J. Stahn, O. Sobolev, A. Hiess, S. Pailhes, C. Baines, N. Momono, M. Oda, M. Ido, and J. Mesot, Phys. Rev. B **78**, 104525 (2008).

[58] T. Goto, S. Kazama, and K. Miyagawa, J. Phys. Soc. Jpn **25**, 3494 (1994).

[59] T. Goto, K. Chiba, M. Mori, T. Suzuki, K. Seki, and T. Fukase, J. Phys. Soc. Jpn **66**, 2870 (1997).